Journal of South American Earth Sciences 104 (2020) 102834

Contents lists available at ScienceDirect

Journal of South American Earth Sciences

journal homepage: www.elsevier.com/locate/jsames

BRAVOSEIS: Geophysical investigation of rifting and volcanism in the Bransfield strait, Antarctica

J. Almendros [a,*], W. Wilcock [b], D. Soule [c], T. Teixidó [a], L. Vizcaíno [a], O. Ardanaz [a], J. L. Granja-Bruña [d], D. Martín-Jiménez [a], X. Yuan [e], B. Heit [e], M.C. Schmidt-Aursch [f], W. Geissler [f], R. Dziak [g], F. Carrión [a], A. Ontiveros [h], R. Abella [i], E. Carmona [a], J.F. Agüí-Fernández [a], N. Sánchez [j], I. Serrano [a], R. Davoli [a], Z. Krauss [b], M. Kidiwela [b], L. Schmahl [c]

[a] University of Granada, Spain
[b] University of Washington, USA
[c] Queens College, CUNY, USA
[d] Complutense University of Madrid, Spain
[e] GFZ Potsdam, Germany
[f] Alfred Wegener Institute, Helmholtz Centre for Polar and Marine Research, Germany
[g] National Oceanographic and Atmospheric Administration, USA
[h] University of Jaen, Spain
[i] National Geographic Institute, Spain
[j] Spanish Geological Survey, Spain

ARTICLE INFO

Keywords:
Bransfield strait
Antarctica
Orca volcano
Humpback volcano
Amphibious seismic network
Marine geophysics
Back-arc basin
Submarine volcano

ABSTRACT

The Bransfield Basin is a back-arc basin located in Western Antarctica between the South Shetland Islands and Antarctic Peninsula. Although the subduction of the Phoenix plate under the South Shetland block has ceased, extension continues through a combination of slab rollback and transtensional motions between the Scotia and Antarctic plates. This process has created a continental rift in the basin, interleaved with volcanic islands and seamounts, which may be near the transition from rifting to seafloor spreading. In the framework of the BRAVOSEIS project (2017–2020), we deployed a dense amphibious seismic network in the Bransfield Strait comprising 15 land stations and 24 ocean-bottom seismometers, as well as a network of 6 moored hydrophones; and acquired marine geophysics data including multibeam bathymetry, sub-bottom profiler, gravity & magnetics, multi-channel seismics, and seismic refraction data. The experiment has collected a unique, high quality, and multifaceted geophysical data set in the Central Bransfield Basin, with a special focus on Orca and Humpback seamounts. Preliminary results confirm that the Bransfield region has slab-related intermediate depth seismicity, with earthquake characteristics suggesting distributed extension across the rift. Gravity and magnetic highs delineate a segmented rift with along-axis variations that are consistent with increased accumulated strain to the northeast. Orca volcano shows evidences of an active caldera and magma accumulation at shallow depths, while Humpback volcano has evolved past the caldera stage and is currently dominated by rifting structures. These differences suggest that volcanic evolution is influenced by the position along the rift. Although a lot of analysis remains, these results provide useful constraints on the structure and dynamics of the Bransfield rift and associated volcanoes.

1. Introduction

Back-arc basins are elongated features that form in subduction settings, behind island arcs and sometimes along continental margins, as a result of extensional processes that are most commonly attributed to slab roll back. They form in two stages, an initial interval of rifting which transitions to a later stage of seafloor spreading. Studies of this process are important for understanding the dynamics and evolution of subduction zones. In locations where back-arc rifting breaks continental crust, this process is also relevant to understanding the formation of

* Corresponding author. Andalusian Institute of Geophysics, University of Granada, C/ Profesor Clavera 12, 18071, Granada, Spain.
E-mail address: vikingo@ugr.es (J. Almendros).

https://doi.org/10.1016/j.jsames.2020.102834
Received 30 July 2020; Received in revised form 20 August 2020; Accepted 21 August 2020
Available online 6 September 2020

passive continental margins (e.g. Martinez et al., 2007; Taylor, 1995).

The Bransfield Basin is a back-arc basin located between the South Shetland Islands and the Antarctic Peninsula in Western Antarctica (Fig. 1). The region is formed by the confluence of several tectonic units, whose limits and interactions are subject to extensive discussions (Pelayo and Wiens, 1989; Lawver et al., 1996; Gracia et al., 1997; Prieto et al., 1998; Gonzalez-Casado et al., 2000; Keller et al., 2002; Barker et al., 2003; Christeson et al., 2003; Fretzdorff et al., 2004; Galindo--Zaldívar et al. 2004, 2006; Maestro et al., 2007; Dziak et al., 2010; Yegorova et al., 2011; Maldonado et al., 2015; Schreider et al., 2015). The Bransfield Basin is somewhat unusual in that the South Shetland Islands have lacked arc volcanism for ~20 Ma (Birkenmajer et al., 1986) and subduction is in the process of ceasing (Lawver et al., 1995). Convergence of the Phoenix plate with the South Shetland Islands stopped at ~3 Ma when seafloor spreading on the Antarctic Phoenix Ridge ceased (Eagles, 2004) but northwest-southeast extension of the Bransfield Basin has continued due to some combination of slab rollback and transtensional motions between the Scotia and Antarctic plates (Lawver et al., 1996; Barker and Austin, 1998; Gonzalez-Casado et al., 2000; Robertson-Maurice et al., 2003; Maestro et al., 2007). In any case, the study of the Bransfield Basin is of broad significance because it is forming in continental crust and may be near the transition from rifting to seafloor spreading. Within current back-arc basins, there are relatively few locations in which the transition from rifting to spreading in continental crust can be observed (e.g. Taylor, 1995). As the only back-arc basin in the Eastern Pacific, it can be considered an analog to the back-arc basins that were once present off much of South America before compression led to the formation of the Andes (Barker et al., 2003).

The Bransfield Strait is composed of three basins aligned in a southwest-northeast direction underlain by continental crust (Grad et al. 1993, 1997; Christeson et al., 2003). The Central Bransfield Basin (CBB) covers an area of about 200 km × 50 km and is located between the main South Shetland Islands and the Antarctic Peninsula and between Deception and Bridgeman Islands. The CBB is probably the most evolved portion of the Bransfield rift, and where extension processes are most important (Galindo-Zaldívar et al., 2004). The area is characterized by a continental rift with thinned crust, or even an incipient oceanic crust (Barker et al., 2003; Galindo-Zaldívar et al., 2004; Catalán et al., 2013). Moho depth estimates in the CBB are diverse, ranging from about 10 km to 30 km (Ashcroft, 1972; Grad et al., 1997; Christeson et al., 2003; Barker et al., 2003; Janik et al., 2006) as a result of disagreements between how to interpret the velocity profiles. Grad et al., (1997) assign velocities of 7.3–7.7 km/s at 14–32 km depth to mafic lower crust with anomalously high velocities and place the Moho at ~30 km where the velocities increase to 8.1 km/s in their model. Christeson et al., (2003) point out that mantle velocities of ~7.5 km/s are feasible in the presence of a few percent melt as might be expected in a rifting environment or with upper mantle anisotropy that resembles that of oceanic lithosphere. Low mantle velocities are also consistent with regional surface wave tomography (Vuan et al., 2005) and P-wave teleseismic travel time tomography (Park et al., 2012) which image structures down to 70 km and 120 km, respectively. On this basis, Barker et al., (2003) and Christeson et al., (2003) measured a crustal thickness of 10–15 km with modern wide-angle ocean-bottom seismometer refraction data. They infer that while there is substantial crustal thinning, the rift is not underlain by normal-thickness (6–7 km) oceanic crust as would be expected if ocean spreading had commenced.

The CBB is strongly asymmetric with the deepest waters (~1500–2000 m) located close to the South Shetland Islands and gentle seafloor slopes near the Antarctic Peninsula. This is reflected in the crustal thickness, which increases rapidly to 20–26 km beneath the South Shetland Islands and more gradually to 14–20 km beneath the margin of the Antarctic Peninsula (Barker et al., 2003; Christeson et al., 2003). Multichannel seismic imaging (Gamboa and Maldonado, 1990; Henriet et al., 1992; Barker and Austin, 1998; Galindo-Zaldívar et al., 2004) shows that the CBB has undergone asymmetric extension. The most extensive study by Barker and Austin (1998) shows that on the South Shetland Islands margin there are closely-spaced, large-offset normal faults. On the Antarctic Peninsula margin, extension is widely distributed, with multiple changes in the dip direction of smaller-offset normal faults as one moves across the strike of the basin. Based on comparisons to other locations, Barker et al., (2003) suggest that trench-side focusing of extension may be a characteristic feature of young back arc basins. Barker and Austin (1998) argue that rifting in the CBB has propagated from northeast to the southwest with an initial episode of extension accompanied by magmatic uplift giving way to subsidence and the formation of low angle northwest dipping detachment faulting beneath the Antarctic Peninsula margin once eruptions commenced in the rift. This coincides with current GPS measurements of relative motions in the Bransfield area (Dietrich et al., 2004; Taylor et al., 2008; Berrocoso et al., 2016). Crustal thickness also tends to thicken from the northeast to southwest consistent with this model of rift propagation (Christeson et al., 2003; Vuan et al., 2005).

It is unclear whether the active rift is a segmented linear structure or a zone of distributed extension. There is evidence of rift segmentation from along axis changes in depth and morphology of the rift (Gracia et al., 1996) and in seismic velocity (Christeson et al., 2003) but these are not well correlated with one another or with the horst and graben structures in the Antarctic Peninsula margin that are inferred to predate the formation of the basin (Christeson et al., 2003). The multichannel data show that there is extensive volcanic basement and rift axis volcanism in the northeast, which gives way to volcanic ridges that are more isolated from one another in the southwest (Barker and Austin, 1998).

The opening of the Bransfield rift has been accompanied by extensive volcanism. Volcanic processes are presently focused along a neovolcanic band perpendicular to the extension direction. Volcanic structures are not exactly aligned, which again relates to the question of whether the rift is a single linear structure or rather affects a distributed area. There are several instances of active subaerial volcanoes in the area. Bridgeman and Penguin Islands (in the NE margin of the CBB) have undergone periods of activity during the past centuries (Fisk, 1990; Smellie, 1990). Deception Island, at the SW limit of the CBB, is also an active volcano with fumarolic emissions, thermal anomalies, deformation processes, and moderate-to-intense seismic activity (Ortiz et al., 1997; Ibáñez et al., 2003; Fernández-Ros et al., 2007; Carmona et al., 2012; Bartolini et al., 2014; Almendros et al., 2018). The eruptive record includes tens of dated eruptions, some of them in historic period, most recently between 1967 and 1970 (Newhall and Dzurisin, 1988; Smellie, 1990; Bartolini et al., 2014). In addition to these subaerial volcanoes, there is a chain of submarine seamounts along the Bransfield Rift. Bathymetric analyses allow the identification of at least six structures in the CBB with a likely volcanic origin (Lawver et al., 1996; Gracia et al., 1997). Moreover, joint interpretations of gravity and magnetic data indicate the presence of shallow magma reservoirs associated with some of these seamounts (Catalán et al., 2013). There is also evidence of strong hydrothermal activity at several points of the Bransfield Basin (Klinkhammer et al., 2001). Rock dredging recovered fresh lavas from numerous sites along the rift (Keller et al., 2002) with chemistries that range from very similar to the nearby arc volcanism to very similar to mid-ocean ridge basalt (MORB). However, the geochemical variations are not systematic along-axis and thus do not provide clear support for the northeast to southwest rift propagation inferred from seismic imaging (Barker and Austin, 1998). The most MORB-like basalts were found on Orca volcano and the Three Sisters where the seismic data suggest a continuous shallow igneous body, but andesite and rhyolite have also been dredged in the same area.

The central part of the basin underlying the Three Sisters and Orca volcano is characterized by a narrower zone of volcanically influenced basement than to the northeast (Barker and Austin, 1998). Upper crustal velocities are also largest in this region, with values as high as 6 km/s at

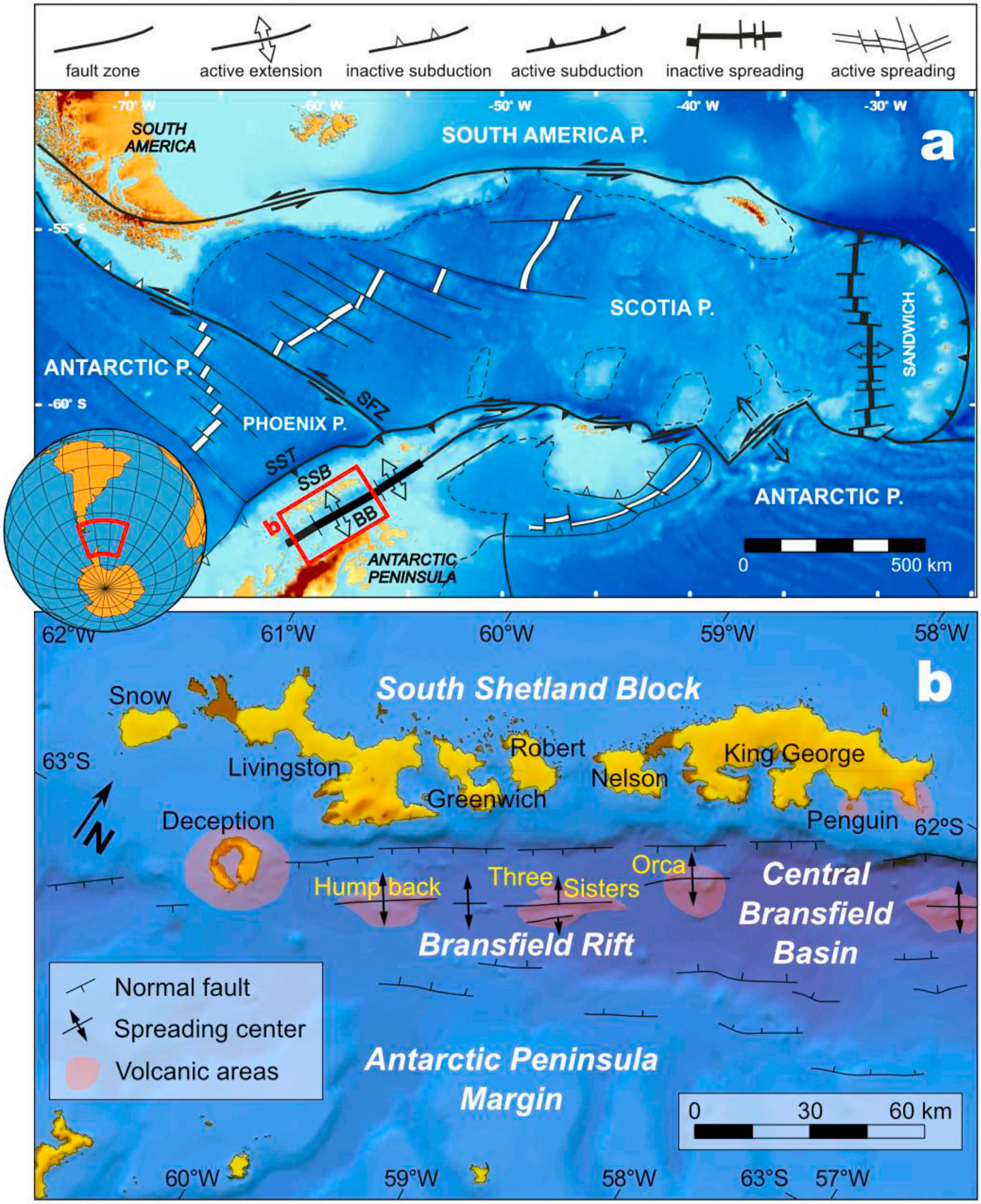

Fig. 1. (a) Map of the Scotia region between South America and Antarctica (see globe inset), showing the main tectonic units and interactions. The red box labeled "b" is the Bransfield Strait area, which is zoomed below. BB: Bransfield Basin; SSB: South Shetland Block; SST: South Shetland Trench. (b) Map of the Bransfield Strait, showing the position of normal faults around the Bransfield Basin, the spreading centers that constitute the Bransfield Rift, and the main volcanic areas (modified from Jiménez-Morales et al., 2017). (For interpretation of the references to color in this figure legend, the reader is referred to the Web version of this article.)

~2 km depth in the vicinity of Orca volcano (Christeson et al., 2003). These results suggest the presence of extensive and possibly continuous shallow igneous material, a feature that has also been inferred from the interpretation of gravity and magnetic data (Catalán et al., 2013; Muñoz-Martín et al., 2005). Indeed, Catalán et al., (2013) argued that the CBB may even be in the very earliest stages of oceanic spreading.

Despite the abundance of prior studies, many questions remain unresolved due to the complex nature of the basin and the historic lack of adequate seismic station coverage. Here we present the first results of the BRAVOSEIS (BRAnsfield VOlcanoes SEISmology) project, an international collaborative effort to investigate submarine volcanoes and rift dynamics in the Bransfield Strait. BRAVOSEIS applies passive and active seismic techniques and complementary geophysical measurements to better characterize the nature of tectonic and volcanic earthquakes in the CBB and link these to the structure of the volcanic rift and extensional basin.

2. Research activities

BRAVOSEIS is a joint project that involves an international group of researchers form different institutions including University of Granada, University of Jaen, Complutense University of Madrid, Spanish Geological Survey, and National Geographic Institute (Spain); University of Washington, CUNY Queens College, and PMEL-NOAA (USA); GFZ Potsdam and Alfred Wegener Institute (Germany). The project developed between 2017 and 2020 using mainly the logistic and technical support of the Marine Technology Unit (CSIC, Spain) and the Spanish Polar Program.

In order to investigate the submarine volcanoes and rift dynamics along the Bransfield Strait, the project incorporates two observational components. The first is the deployment of a dense, amphibious seismic network, comprising both land and ocean bottom seismometers and moored hydrophones. This network allows the investigation of different seismological aspects of the Bransfield area, such as the crustal and upper mantle structure, the geometry and dynamics of faults and their relation to the Bransfield Rift, the shallow structure of volcanic edifices, and the prevalence of volcanic seismicity in the area. The second component is the collection of a set of marine geophysics profiles, in order to add to regional scale observations for the Bransfield Strait and explore in detail the shallow rift structure over selected sites. The techniques applied include multichannel seismic reflection profiles, refraction studies, gravity and magnetic measurements, sediment profiler data, and multibeam bathymetric soundings.

All these activities were carried out within the framework of the Spanish Antarctic Campaigns in 2017–2018, 2018–2019 and 2019–2020. The timeline of the project is shown in Fig. 2. The BRAVOSEIS 2018 cruise was undertaken by the R/V Hesperides in February-March 2018 and deployed a portion of the land stations. The BRAVOSEIS 2019 cruise took place in January 2019 on the R/V Sarmiento de Gamboa and carried out the deployment of the remaining land instruments and all marine instruments, and obtained most of the geophysics profiles including active seismics. During this field season, the Hesperides also helped support the maintenance of land seismic stations. The BRAVOSEIS 2020 cruise was conducted by the R/V Hesperides in February 2020. It recovered all land and marine stations, and acquired geophysical data along a few more profiles.

2.1. Deployment of the amphibious seismic network

The first objective of the field operations was the deployment of a dense, amphibious seismic network in the Bransfield Strait area. Land instruments included 12 seismic stations equipped with 120-s Nanometrics Trillium Compact seismometers and Cube3 data acquisition systems sampling at 50 sps, provided by DEPAS (German Instrument Pool for Amphibian Seismology, AWI et al. 2017). Seismometers were buried at a depth of about 50 cm, in a protecting box providing

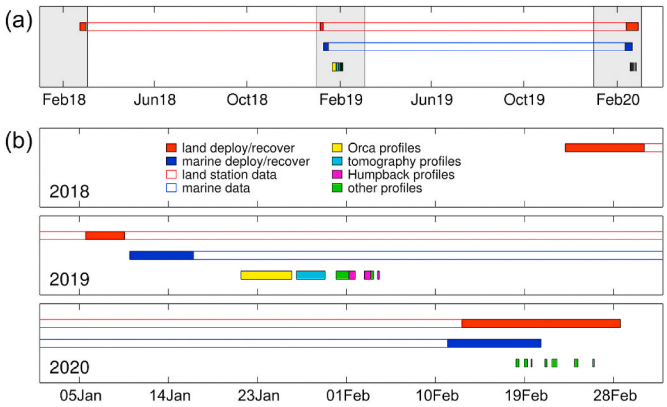

Fig. 2. Timeline of the BRAVOSEIS operations for the full project duration (a) and for each of the three cruises (b). The shaded areas in (a) correspond to the periods zoomed in (b). In all panels, filled boxes indicate the activities related to the land stations (top row, red), marine stations (middle row, blue), and geophysics profiles (bottom row, multiple colors indicating the work area). Empty boxes indicate the autonomous operation of the land and marine networks. (For interpretation of the references to color in this figure legend, the reader is referred to the Web version of this article.)

insulation for temperature changes and water influx. The power supply was based on a pack of long-duration air-alkaline batteries (4 × 6 V, 600 Ah), which are able to keep the system powered for up to two years. Therefore, the stations are autonomous and do not depend on external energy sources (solar panels or wind generators), which results in a compact and robust deployment (Fig. 3a). Additionally, we used three permanent seismic stations deployed by University of Granada in 2008 (project CORSHET, POL2006-08663, https://doi.org/10.7914/SN/B6) and maintained during the past years with assistance from other research projects (e.g. Carmona et al., 2014). Two of these stations (DCP and LVN) were upgraded with 120-s Nanometrics Trillium Posthole seismometers and Nanometrics Centaur dataloggers sampling at 100 sps. The remaining station (CCV) used a 16-s EENTEC SP400 seismometer, with an EENTEC DR4000 datalogger sampling at 100 sps. In these three stations, power supply was provided by a combination of solar panels and lead-acid batteries. Land instruments were deployed at locations around the Central Basin of the Bransfield Strait, both in the South Shetland Islands and the Antarctic Peninsula margin (Fig. 4). They were deployed in two stages (Table 1). Between February 25 and March 2, 2018 we deployed five temporary land stations and upgraded two of the permanent stations. The remaining land stations could not be deployed that season, because the survey was abruptly cancelled due to a tragic accident. The deployment of the seven remaining land stations was performed between January 5–9, 2019, at the beginning of the BRAVOSEIS 2019 cruise.

Marine stations comprised 6 hydrophone moorings, 9 broadband OBS, and 15 short-period OBS (Fig. 3b). Hydrophone moorings were based on ITC-1032 ceramic omnidirectional acoustic sensors combined with a 16-bit NOAA datalogger sampling at 1000 sps. They were deployed on both sides of the rift axis, in a configuration very similar to the network used by Dziak et al., (2010). The moorings had an anchor, acoustic release, and a length of line sufficient to keep the hydrophone and float at a depth of ~500 m below the sea surface out of the expected reach of icebergs. The OBS were distributed in a nested configuration (Fig. 4). Broadband instruments were Kum Lobster OBS with 120-s Nanometrics Trillium Compact seismometers, HTI-04 hydrophones, and Kum 6D6 dataloggers sampling at 100 sps (AWI et al. 2017). They were deployed across the basin with an aperture of ~200 km and inter-station distances of ~30 km. The resulting broadband network (combining land and marine stations) is therefore designed for studies of regional tectonics and crustal and uppermost mantle structures. Short-period instruments were WHOI D2 OBS equipped with 4.5-Hz

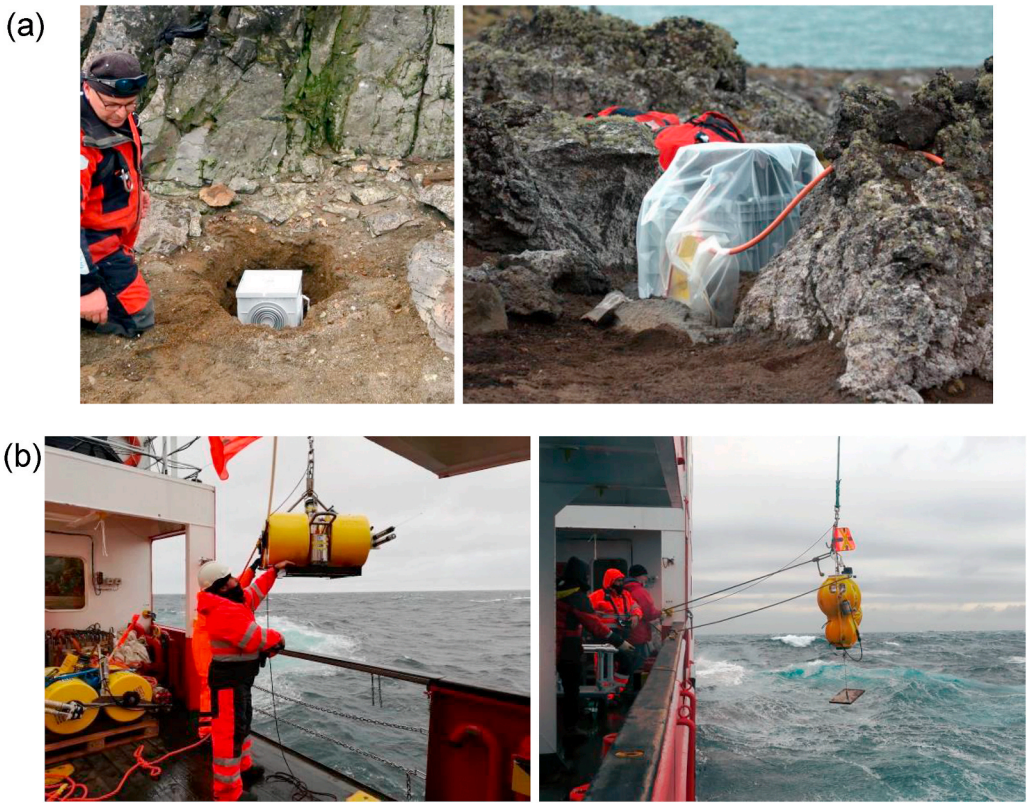

Fig. 3. (a) Installation of a land seismometer inside a buried protecting case at Snow Island (left) and final aspect of the battery pack and acquisition system (height ~0.6 m) of station PEN at Penguin Island (right). (b) Deployment of broadband (left) and short-period (right) OBS during the BRAVOSEIS 2019 cruise.

Geospace GS-11D geophones, HTI-90 hydrophones, and Quanterra Q330 dataloggers sampling the vertical and hydrophone channels at 200 sps and the horizontal channels at 100 Hz. They were clustered around Orca volcano and its SW rift, covering a region of 20 km × 10 km, with inter-station distances of ~4 km. This dense network is intended for detailed studies of the volcanic seismicity and structure. OBS depths range from 770 m (stations located on top of Orca volcano) to 1940 m (stations in the deepest portion of the Central Bransfield Basin, east of Orca volcano). Marine instruments were deployed from January 10–16, 2019 (Table 2) during the BRAVOSEIS 2019 cruise, and collected data for just over one year.

In the BRAVOSEIS 2020 cruise (between February 12–29, 2020) we recovered all the seismic instruments. Station performance has been generally satisfactory (Fig. 4). Land stations were mostly in working operation, even though in some cases the insulation seals had not held and some instruments had suffered from the interaction with ice and thaw water. Stations DCP and LVN suffered a power shortage during the austral winter, and recorded only during the summer. Surprisingly for Antarctica, the data acquisition system of station CCV had been stolen from its protecting case, resulting not only in the loss of the datalogger, but the loss of one year of seismic data from when the station was last visited in February 2019. These problems imply that the data return rate has been just 57% for these stations. On the contrary, GFZ stations based on the Cube3 datalogger only lost some data in early 2019, due to the overwriting of existing files. The data return has been excellent, near 93% of the deployment time. The marine instruments were also recovered in working condition, except for two OBS (one broadband and one short-period) that were lost because the acoustic releases did not respond to transducer signals. One short-period OBS stopped recording about a month before the end of the deployment because the batteries had depleted, and the seismometer of BRA03 malfunctioned after mid-July 2019. Otherwise, all the OBS returned full data sets. In spite of this, the data return rates are high: 84% for the broadband OBS; 93% for the short-period OBS; and 100% for the hydrophones.

2.2. Marine geophysics surveys

The second objective of the project was a set of marine geophysics profiles over different target structures. These were mostly carried out during the BRAVOSEIS 2019 cruise, between January 18 and February 4, 2019. Some profiles could not be collected due to the presence of a large iceberg. Therefore in the BRAVOSEIS 2020 cruise, between February 18–26, 2020 we obtained a few extra profiles to complete our dataset. Unfortunately these did not include active seismics, which were not available during the 2020 cruise. The ship tracks can be seen in Fig. 5.

We mapped the seafloor bathymetry and shallow sediment structure using a multibeam echosounder ATLAS Hydrosweep DS and a sediment profiler ATLAS Parasound P-35. For the additional 2020 profiles, we used a multibeam sounder Kongsberg EM122 and sediment profiler Kongsberg TOPAS PS18. Gravity data were acquired continuously using gravity meters mounted on a gyro-stabilized platform for damping of ship movements. A Lacoste & Romberg Air-Sea System III gravimeter and a Bell Aerospace Textron BGM-3 model were used during the BRAVOSEIS 2019 and 2020 cruises, respectively. In both cases, we used a sampling interval of 1 s and an accuracy of ±1 mgal. Relative gravity measurements were linked to the on-land absolute gravity network by means of a terrestrial CG-5 microgravity meter, following the procedure described by Carbó et al., (2003). The absolute gravity benchmarks were Punta Arenas (Chile) and Vigo (Spain) for the 2019 cruise and Ushuaia (Argentina) and Punta Arenas (Chile) for the 2020 cruise. The strength of the magnetic field was measured using a proton-precession, Marine Magnetics SeaSPY 300 M magnetometer, with a sampling interval of 1 s and an accuracy of ±0.2 nT. Magnetic data were acquired along navigation lines, with the instrument towed sternward at a distance of 200 m. During the whole period, time and position were determined via an

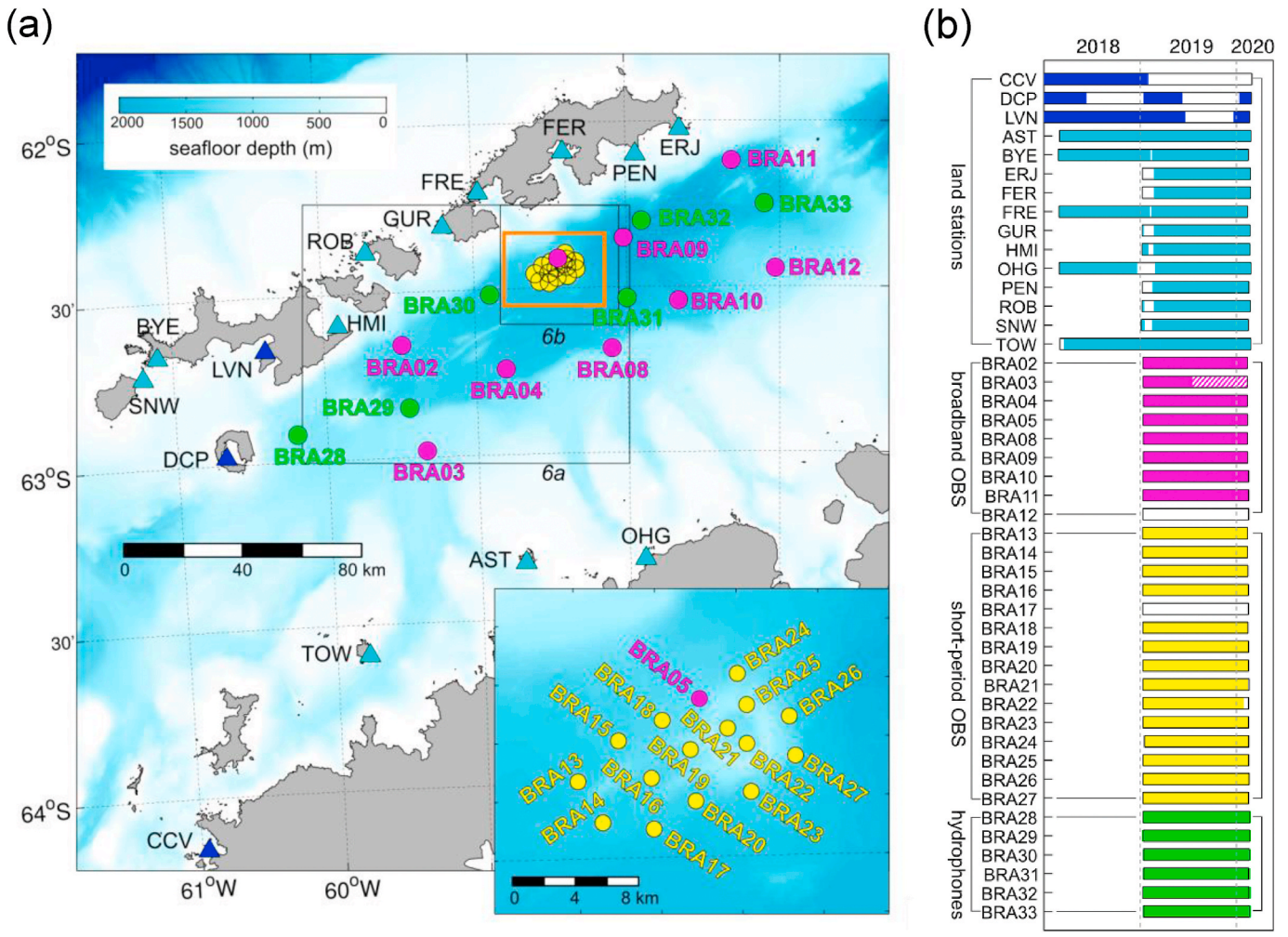

Fig. 4. (a) Seismic network deployed in the Bransfield Strait during 2018/2019–2020. Land stations are shown as triangles, with color representing the station types: cyan for GFZ stations, blue for UGR stations. Ocean stations are displayed as circles, with colors representing station types: yellow for WHOI OBS, magenta for AWI OBS, green for NOAA hydrophones. The inset shows a detail of the OBS network around Orca volcano, marked in the main map by the orange box. The black boxes labeled 6a and 6 b correspond to the areas shown in Fig. 6a and b, respectively, where we have focused the marine geophysics investigations. (b) Performance of the seismic stations. Black boxes outline the deployment period, and colored boxes indicate the data retrieved, with the same color code as above. The stripped pattern in BRA03 indicates partial loss of data due to malfunction of the seismometer. (For interpretation of the references to color in this figure legend, the reader is referred to the Web version of this article.)

Table 1
List of land stations deployed in the BRAVOSEIS project, including station name, coordinates, date of deployment, date of recovery, and instrument type.

Name	Latitude	Longitude	Date installed	Date recovered	Type
AST	63°19.636′S	58°42.160′W	2018-03-01	2020-02-24	GFZ
BYE	62°39.990′S	61°05.953′W	2018-02-25	2020-02-14	GFZ
ERJ	62°01.462′S	57°38.947′W	2019-01-09	2020-02-22	GFZ
FER	62°05.386′S	58°24.393′W	2019-01-08	2020-02-22	GFZ
FRE	62°12.408′S	58°57.640′W	2018-02-28	2020-02-12	GFZ
GUR	62°18.452′S	59°11.758′W	2019-01-08	2020-02-21	GFZ
HMI	62°35.748′S	59°54.232′W	2019-01-07	2020-02-20	GFZ
OHG	63°19.327′S	57°53.839′W	2018-03-01	2020-02-25	GFZ
PEN	62°05.959′S	57°56.204′W	2019-01-08	2020-02-16	GFZ
ROB	62°22.761′S	59°42.212′W	2019-01-07	2020-02-21	GFZ
SNW	62°43.672′S	61°12.019′W	2019-01-05	2020-02-14	GFZ
TOW	63°35.525′S	59°46.965′W	2018-03-02	2020-02-24	GFZ
CCV	64°09.348′S	60°57.372′W	2008-02-01	2019-01-24	UGR
DCP	62°58.650′S	60°40.692′W	2008-02-12	2020-02-26	UGR
LVN	62°39.762′S	60°23.250′W	2008-02-05	2020-02-19	UGR

integrated differential GPS system with an average accuracy of 1–2 m.

Finally, seismic data were obtained using two different setups for reflection and refraction studies, respectively. We acquired multi-channel seismic (MCS) data using a Sercel Sentinel streamer with 120 channels and an active section of 1500 m, with a spacing between channels of 12.5 m. The streamer was set at a depth of 5 m. We used a window length of 14 s and a sampling interval of 2 ms (500 sps). The seismic source was an array of Sercel GGUN-II airguns with a total capacity of 29.2 l (1780 c.i.). This capacity was later reduced to 25.9 l (1580 c.i.) due to repeated failures of the 250 c.i. guns, which forced us to replace the 250 c.i. guns with 150 c.i. guns. The source array was towed at a depth of 5 m as well. The ship speed was 4 knots and the shooting interval was 37.5 m (about 15 s), to allow for the recharge of the guns between shots.

The MCS profiles were most dense over two of the volcanic structures of the Bransfield rift. The first one is Orca, a seamount located about 20 km south of King George Island (Fig. 1). The second one is a volcanic edifice located 20 km east of Deception Island, identified as Edifice A in Gracia et al., (1996), that we propose to name Humpback volcano in consonance with its neighbor Orca volcano, its striking shape, and as a homage to another whale species common in this area. We carried out

Table 2
List of marine instruments deployed in the BRAVOSEIS project, including station name, coordinates, date of deployment, date of recovery, and instrument type.

Name	Latitude	Longitude	Date installed	Date recovered	Type
BRA02	62°39.594′S	59°29.184′W	2019-01-12	2020-02-11	AWI
BRA03	62°58.860′S	59°20.616′W	2019-01-12	2020-02-11	AWI
BRA04	62°44.478′S	58°48.216′W	2019-01-12	2020-02-11	AWI
BRA05	62°24.618′S	58°26.874′W	2019-01-11	2020-02-12	AWI
BRA08	62°41.070′S	58°06.156′W	2019-01-13	2020-02-11	AWI
BRA09	62°21.054′S	58°01.140′W	2019-01-13	2020-02-12	AWI
BRA10	62°32.508′S	57°39.816′W	2019-01-11	2020-02-16	AWI
BRA11	62°07.182′S	57°18.774′W	2019-01-11	2020-02-16	AWI
BRA12	62°26.706′S	57°01.656′W	2019-01-11	lost	AWI
BRA13	62°27.400′S	58°35.811′W	2019-01-10	2020-02-12	WHOI
BRA14	62°28.843′S	58°34.143′W	2019-01-10	2020-02-12	WHOI
BRA15	62°26.017′S	58°32.665′W	2019-01-10	2020-02-12	WHOI
BRA16	62°27.339′S	58°30.364′W	2019-01-10	2020-02-15	WHOI
BRA17	62°29.034′S	58°30.432′W	2019-01-10	lost	WHOI
BRA18	62°25.274′S	58°29.398′W	2019-01-11	2020-02-13	WHOI
BRA19	62°26.328′S	58°27.504′W	2019-01-11	2020-02-15	WHOI
BRA20	62°28.107′S	58°27.189′W	2019-01-11	2020-02-15	WHOI
BRA21	62°25.602′S	58°24.781′W	2019-01-11	2020-02-17	WHOI
BRA22	62°26.193′S	58°23.473′W	2019-01-11	2020-02-15	WHOI
BRA23	62°27.810′S	58°23.049′W	2019-01-11	2020-02-15	WHOI
BRA24	62°23.702′S	58°23.910′W	2019-01-16	2020-02-17	WHOI
BRA25	62°24.891′S	58°23.647′W	2019-01-12	2020-02-17	WHOI
BRA26	62°25.266′S	58°20.365′W	2019-01-12	2020-02-17	WHOI
BRA27	62°26.543′S	58°19.869′W	2019-01-12	2020-02-15	WHOI
BRA28	62°54.908′S	60°11.979′W	2019-01-12	2020-02-20	NOAA
BRA29	62°50.997′S	59°27.015′W	2019-01-12	2020-02-20	NOAA
BRA30	62°30.951′S	58°53.988′W	2019-01-13	2020-02-18	NOAA
BRA31	62°32.003′S	58°00.047′W	2019-01-13	2020-02-15	NOAA
BRA32	62°17.846′S	57°53.671′W	2019-01-10	2020-02-17	NOAA
BRA33	62°14.989′S	57°05.987′W	2019-01-13	2020-02-18	NOAA

18 parallel MCS profiles over Orca volcano (555 km), with a distance between profiles of 500 m; 11 parallel profiles over Humpback volcano (182 km), spaced 1 km; 4 profiles across the Bransfield rift (78 km) at distances of ~10 km; and 7 additional profiles (107 km). This adds up to a total of 40 MCS profiles (922 km). The profile locations are shown in Fig. 6. Most profiles are oriented NW-SE, perpendicular to the rift direction, except for the additional profiles that have been taken parallel to the rift. The dense sets of profiles over the two submarine volcanic edifices are intended for 3D interpretation. Originally more profiles were planned across the rift between Orca and Humpback seamounts, particularly in the central part above Three Sisters ridge. However, the presence of a very large iceberg and poor weather prevented us from completing these profiles.

Additionally, we generated seismic signals over Orca volcano, to be recorded by the OBS network and used for tomography and refraction studies. For this, we selected an airgun configuration with total capacity of 41.6 l (2540 c.i.) at a depth of 15 m. The ship navigated at 4 knots and the shooting interval was 200 m (around 95 s), to allow for the extinction of the signal before the next arrival. We shot 28 lines totaling 485 km (Fig. 6) and ~2400 shots distributed in an area of 20 km × 10 km, with higher density in the central part above the volcano.

3. Preliminary results and discussion

3.1. Seismic network

The Bransfield Strait is a seismically active region, with earthquakes as large as M7 (in 1971) and 45 earthquakes larger than M5 in the last 50 years (International Seismological Centre, 2020). However, the scarcity of permanent seismic stations in the South Shetland Islands and Antarctic Peninsula limits seismic catalogs to earthquakes with magnitudes above ~4. Most of them have shallow hypocenters and normal or strike-slip mechanisms, which are consistent with the extensional tectonic regime of the area (Pelayo and Wiens, 1989; Gonzalez-Casado et al., 2000).

Several temporary deployments have allowed the analysis of the seismicity with enhanced station coverage. For example, Robertson-Maurice et al., (2003) deployed 7 seismic stations and 14 OBS in the South Shetland Islands region between 1997 and 1999. Their catalog contains ~150 well-located earthquakes with body wave magnitudes from 2 to 5 (mostly >3). The locations and mechanisms of some of these earthquakes suggest that there is continued subduction-related seismicity at shallow and intermediate depths (Ibáñez et al., 1997; Robertson-Maurice et al., 2003). Additionally, the catalog includes several clusters of shallow earthquakes spatially associated with submarine volcanic edifices. A group of earthquakes on the flank of Orca Volcano

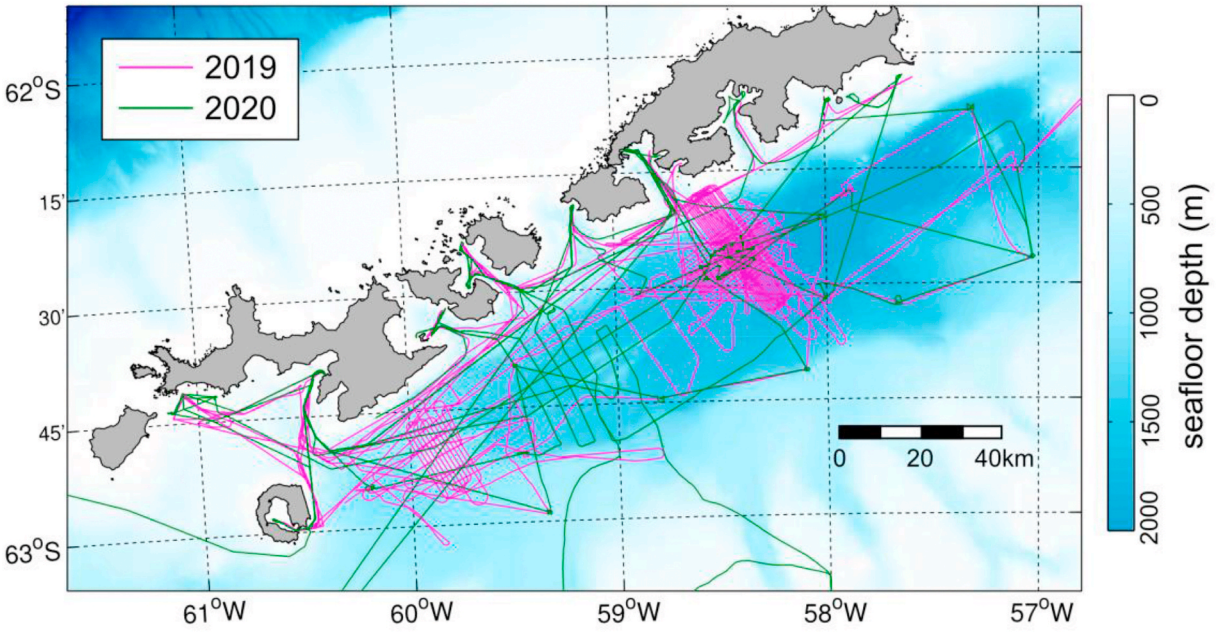

Fig. 5. Ship tracks during the BRAVOSEIS 2019 (magenta) and 2020 (green) cruises. (For interpretation of the references to color in this figure legend, the reader is referred to the Web version of this article.)

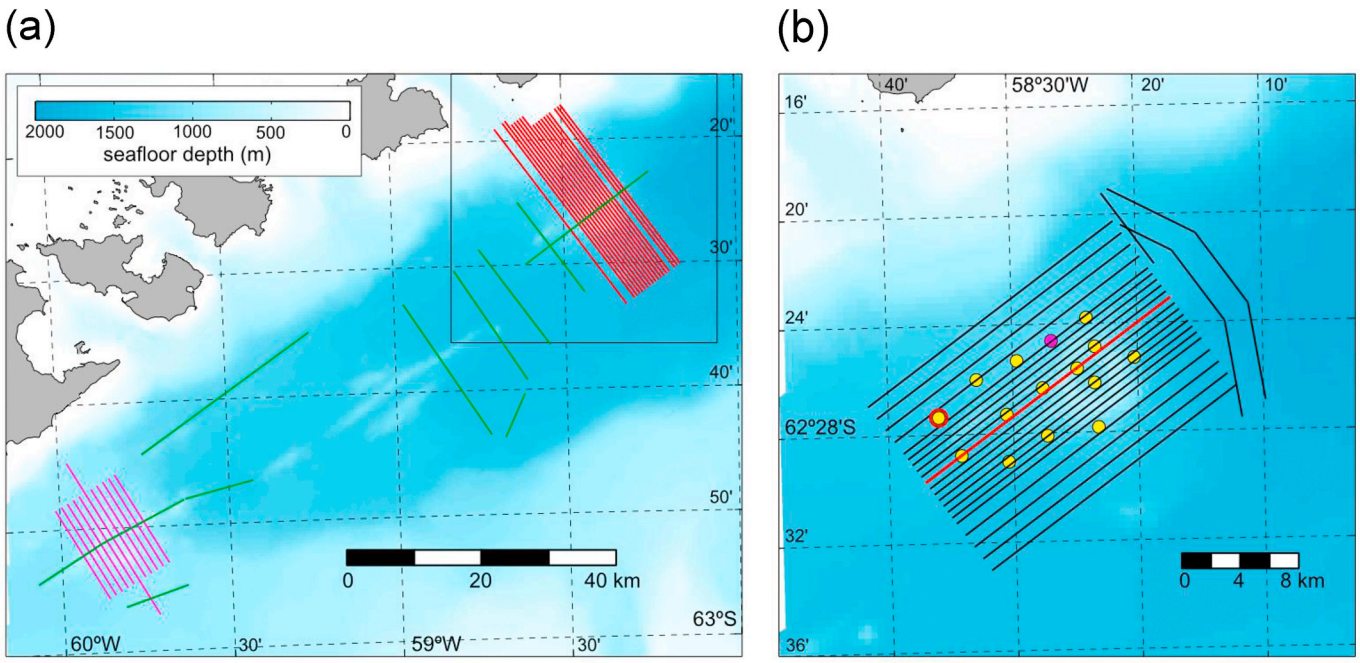

Fig. 6. (a) MCS profiles carried out over Orca volcano (red), Humpback volcano (purple), and in the Bransfield rift (green). (b) Shooting profiles carried out over the seismic instruments surrounding Orca volcano (black), for tomography and refraction studies. The shots of the profile marked in red, recorded at the OBS encircled in red, are displayed in Fig. 15. The area zoomed in (b) is marked by a black box in (a). (For interpretation of the references to color in this figure legend, the reader is referred to the Web version of this article.)

were interpreted as possibly indicative of magmatic or eruptive activity. Dziak et al., (2010) used a network of 5–7 hydrophones to investigate the seismic activity in the CBB between 2005 and 2007. Their catalog of ~3900 earthquakes with estimated magnitudes mostly ≤2, is dominated by earthquakes near the rift and their distribution suggests that it is active along its length. Several clusters of earthquakes are again spatially associated with volcanic structures including Hook Ridge (SW of Bridgeman Island), Orca Volcano, the parallel ridges of the Three Sisters, and Deception Island. The seismicity at Deception Island volcano has been extensively studied in the last 30 years using seismic arrays and local networks (Ortiz et al., 1997; Almendros et al. 1997, 1999, 2015, 2018; Ibáñez et al. 2000, 2003; Carmona et al. 2012, 2014). Seismic episodes of volcano-tectonic earthquakes rising above the background levels have been reported in 1992, 1999, and 2015 (Ortiz et al., 1997; Ibáñez et al., 2003; Almendros et al., 2018). In addition, Almendros et al., (2018) describes a series of earthquakes located southeast of Livingston Island in 2014–2015, some of which were large enough to be located by global networks. Although the location uncertainties are large, their positions and temporal evolution suggest a relationship with submarine volcanic structures. The series may have lasted until 2016, when Dimitrova et al., (2017) identified a cluster of earthquakes in the same epicentral area, using a three-component station deployed at the Bulgarian Base in Livingston Island.

The BRAVOSEIS network constitutes an improvement in the seismic coverage of the area, and significant results are anticipated. Seismic data from the complete amphibious network were retrieved in the 2020 cruise, and are being curated and organized. However, data from the 8 land stations operating in 2018 were downloaded during the 2019 cruise and have been preliminarily processed and analyzed using routine techniques. Station performance was satisfactory, and in 5 cases the data span the entire deployment period. Station CCV recorded during the entire period, but there was a timing problem and the data are not useable for some applications. Station DCP had a problem with the power supply and stopped in June 2018. Finally, station AST failed in November 2018, due to a power shortage produced by a break in the insulation from water and ice, and was only replaced in February 2019. Our dataset was completed with seismic data from the permanent station JUBA belonging to the Antarctic Seismograph Argentinian Italian Network (ASAIN, https://doi.org/10.7914/SN/AI). This station is located near Base Carlini (Argentina) in King George Island. An additional ASAIN station ESPZ, located in Base Esperanza (Argentina) near the NE tip of the Antarctic Peninsula, could not be used due to timing problems.

In order to explore the dataset for significant earthquakes, we used an automated event detection method based on the STA/LTA ratio, specifically the CONDET routine provided with the SEISAN software package (Ottemöller et al., 2017). After several tests to fine-tune the detection parameters (Davoli, 2019), we identified a set of 227 tectonic earthquakes (Fig. 7). The largest earthquake recorded in the area had a magnitude of 5.6, and nine earthquakes had magnitudes larger than 3. The remaining earthquakes were characterized by magnitudes in the range 0.5–3. We estimated source locations based on P and S phase arrival times, using an average velocity model for the Bransfield Strait area (Christeson et al., 2003; Ben-Zvi et al., 2009; Zandomeneghi et al., 2009). Source mechanisms were obtained using the FPFIT software included in SEISAN, which is based on the polarity of the first P-wave arrivals.

Fig. 8 shows an epicentral map of the earthquakes, color-coded by depth range. Seismicity is scattered all over the Bransfield Strait area, although earthquakes occur predominantly within a NE-SW elongated band containing the South Shetland Islands. Several earthquakes occur between the South Shetland Trench and the South Shetland Islands, with depths that generally increase further from the trench. Seismicity along the Bransfield rift seems to be discontinuous, consistent with a complex structure of offset segments rather than a continuous, linear rift. We find some clusters of shallow earthquakes, for example in the Central Bransfield Basin or west of Deception Island. Dziak et al., (2010) described similar clusters in 2005–2007, and related them to the activity of volcanic centers in the area. In our case, two of the clusters coincide with Deception Island and Orca volcano. Another cluster is located near the SW tip of the Three Sister ridge. However, there is no evidence of volcanic features corresponding to the westernmost cluster, that could

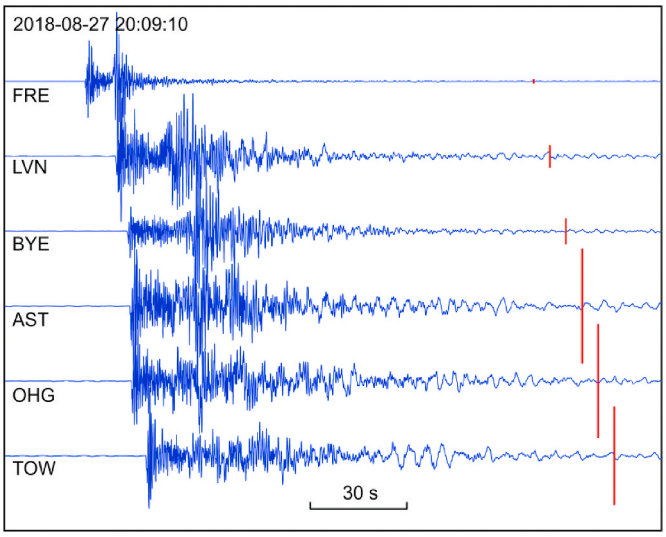

Fig. 7. Seismograms (vertical component) of a M5.6 tectonic earthquake recorded by land seismometers in the Bransfield Strait area on August 27, 2018. Data are normalized to their maxima; the red bars on the right side indicate the relative seismogram amplitudes. The start time of the records is indicated at the top left. (For interpretation of the references to color in this figure legend, the reader is referred to the Web version of this article.)

be related instead to transverse faults linking the SW sections of the rift. Finally, there is also some seismicity south of the Bransfield Rift. Several earthquakes appear within the limits of the Antarctic Peninsula shelf. These may correspond to shallow faults that have been reported in studies of the shallow structure (e.g. Galindo-Zaldívar et al., 2004). It is noteworthy that a few earthquakes are located in the Antarctic Peninsula. They are characterized by small magnitudes and shallow depths. Given their characteristics, they could be either small tectonic earthquakes or seismic events generated by glaciers. These areas were not previously identified as seismically active, which is most likely due to the lack of seismic station coverage. In any case, a more detailed analysis is required to assess the origin of these earthquakes.

Most earthquakes have source depths extending down to 30 km. This coincides with Moho depth estimates in the area, which are nevertheless highly variable, ranging from 15 to 40 km (Grad et al., 1997; Vuan, 2001; Christeson et al., 2003; Janik et al., 2006; Biryol et al., 2018; Parera-Portell et al., 2020). There are also a significant number of intermediate earthquakes with depths of 30–140 km at ranges of >100 km from the trench. Similar observations were reported by Ibáñez et al., (1997) and Robertson-Maurice et al., (2003), and interpreted as evidence of active subduction processes in the convergence between the Drake section of the Antarctic Plate and the South Shetland microplate.

Finally, we have attempted to calculate source mechanisms. They are not very robust given the sparse distribution of stations and generally small magnitudes. Fig. 8 shows two examples of focal mechanisms corresponding to a shallow earthquake near the rift, and an intermediate-depth earthquake near the trench. In general, earthquakes near the rift are better constrained, and clearly display an important

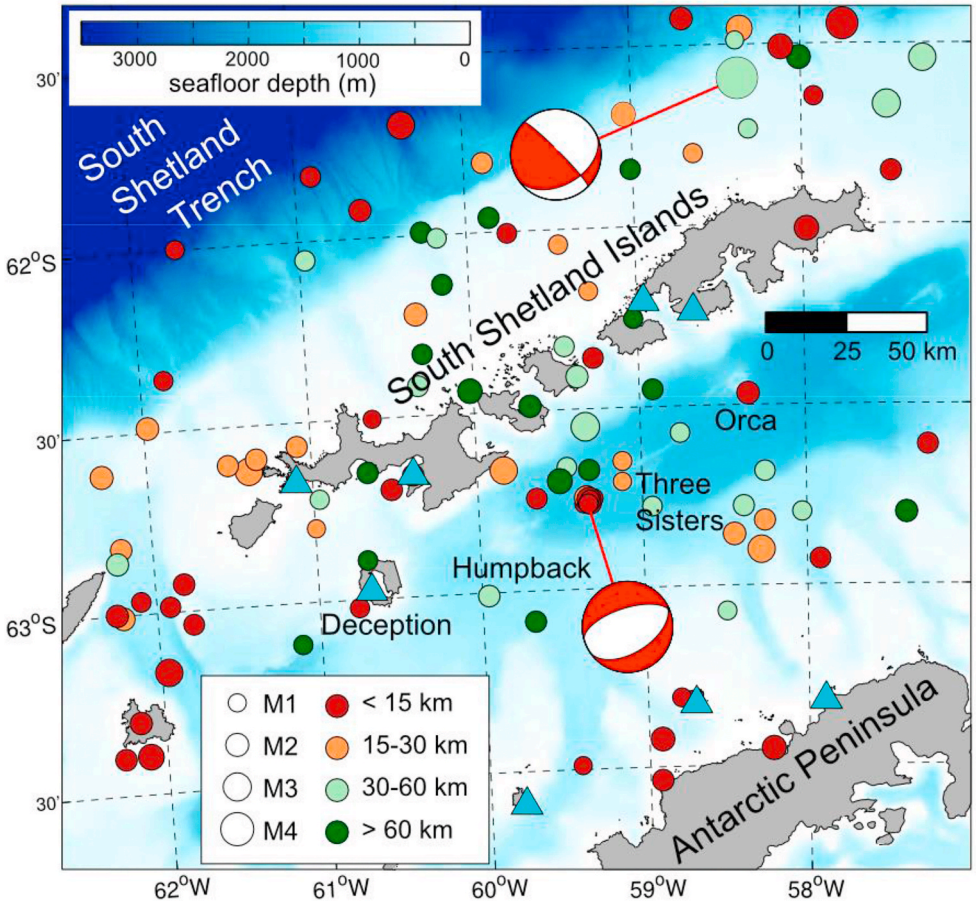

Fig. 8. Epicentral map showing the locations of the earthquakes recorded during 2018 (circles) color-coded by depth. Symbol sizes indicate the earthquake magnitudes. The triangles represent the positions of the seismic stations operating during this period. (For interpretation of the references to color in this figure legend, the reader is referred to the Web version of this article.)

normal fault component corresponding to a region under extensional stresses. Although poorly constrained, earthquake mechanisms near the South Shetland Trench do not indicate normal faulting, but a combination or strike-slip and reverse motions. Therefore both the spatial distribution of earthquakes and the source mechanisms seem to support the subduction of the Antarctic Plate under the South Shetland block, with the associated back-arc extension due to slab roll-back.

3.2. Bathymetry and sediment profiler

The first bathymetric maps specifically focused on the Bransfield Strait were obtained in the early 90s (Kepleis and Lawver, 1994; Gracia et al., 1996). Although their resolutions were limited by the data coverage and swath overlap, they imaged significant features, for example the asymmetry of the basin, and the presence of volcanic seamounts and submarine ridges (Gracia et al., 1997; Lawver et al., 1996). More exhaustive analyses of the seafloor topography were performed

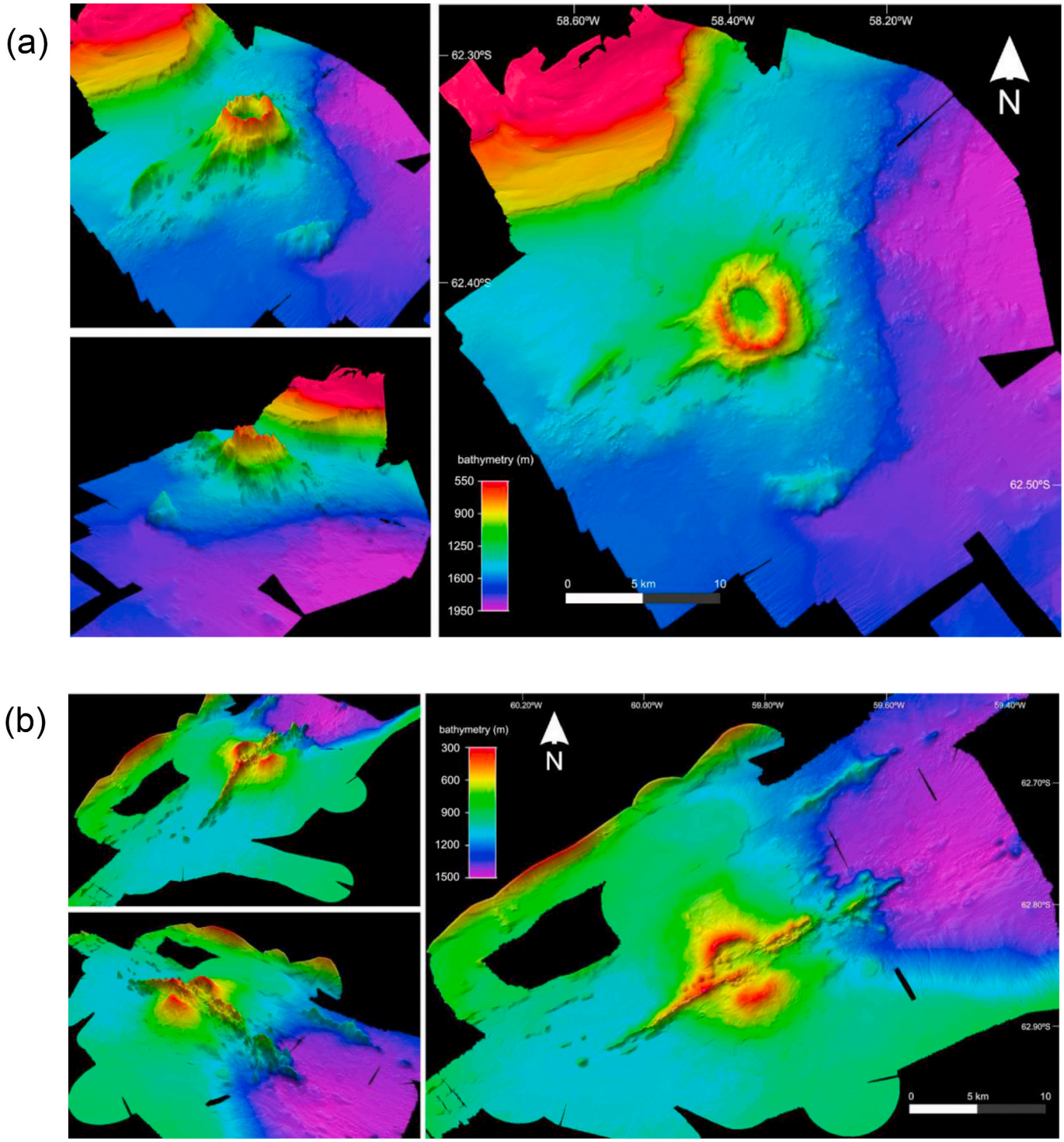

Fig. 9. (a) Bathymetry of Orca volcano. The panels show a view from the SW (top left), a view from the SE (bottom left), and a map view (right). Vertical exaggeration in the side views is 5. (b) Same as (a) for Humpback volcano.

after the TOMODEC experiment in 2005 (Ibáñez et al., 2017), when the detailed seafloor features around Deception Island volcano were investigated using high-resolution bathymetry data (Barclay et al., 2009).

Our bathymetry data covers a large portion of the Central Bransfield Basin, however its main strength is the high density of profiles in two volcanic areas: Humpback and Orca. Raw multibeam data obtained along the ship tracks in the BRAVOSEIS 2019 and 2020 cruises have been processed using the CARIS software, provided by the cooperation with the Marine Technology Unit (UTM) and TRAGSATEC. The data are optimal in the Orca and Humpback zones, where there is extensive swath overlap. In these areas, we have obtained digital elevation models of the seafloor with a resolution of 15 m, and spatial extents of about 35 km × 25 km (Fig. 9).

The results show that Orca volcano is a 4-km wide caldera, slightly elongated in NW-SE direction. The basal diameter is about 7.5 km, and the volcanic edifice occupies an approximate area of 45 km^2. The caldera rim reaches a maximum elevation of −610 m in the South side. With the surrounding seafloor at average depths of 1500 m, Orca volcano rises ~900 m from the seafloor. The northern caldera rim is irregular and has generally lower elevations of about −800 m. There is a breach in the rim to the NE, reaching a depth of 900 m. The caldera floor has an average elevation of −1080 m, about 420 m above the surrounding seafloor and 300–400 m below the caldera rim. Linear ridges radiate from the caldera in multiple directions with two prominent ridges to the SW (the rift direction) and others to the W and N. There is a deep (~80 m) moat beneath the northern half of the caldera rim that suggests that the caldera may have recently undergone resurgence. Alternatively, this moat could be related to contouritic effects. In the South, there is a secondary volcanic cone with an elevation of −740 m, rising about 340 m from the caldera floor. A volcanic topographic high that parallels the rift direction is located 9 km to the SSE. To the NW, the South Shetland shelf has depths shallower than −800 m, dropping to a minimum elevation of −1300 m at the base of the seamount. Orca volcano marks the transition towards the deepest portion of the Central Bransfield Basin, with depths of 1640 m to the SW and up to ~1950 m to the NEE. Flank slopes reach up to 25-30°. There are some small landslide structures on the NW flank, and a large slide on the SE side, starting at a depth of about −900 m. The lobated slide deposit is clearly visible, with a basal width of about 2 km.

In comparison to Orca Volcano, Humpback volcano is a lower and wider edifice that rises about 500 m above the surrounding seafloor. The basal diameter is 16 km, and the total area occupied by the volcanic edifice is about 200 km^2. The volcano has the shape of a circular caldera with a diameter of 5 km, cut by a 30-km-long linear ridge in a NE-SW direction that coincides with the rift direction. The maximum elevations are −380 m in the NW caldera rim and −340 m in the ridge. Maximum slopes are ~25° at the summit and 32° on the ridge. There are about 15 small volcanic cones scattered within the caldera, with diameters of 100–300 m. Lava flows with a maximum length of 2 km are visible along the ridge. Isolated volcanic cones with diameters up to 1 km are also present at both ends of the ridge.

Although Orca and Humpback volcanoes are both located on the Bransfield rift, only 90 km apart, they have quite different characteristics. Orca has a round, flat caldera, with ridges radiating away from the center in several directions. Humpback seamount is broken by a large ridge, and the caldera floor is crowded with small monogenetic volcanic cones. Humpback caldera was clearly formed before the ridge that pushed the two halves apart. No significant shear motion is evident from the positions of the two caldera halves, indicating that the lateral (along the rift) motions are small compared to the extension rate.

Sediment profiler data allow us to complement the information from the bathymetry. We have used the SonarWiz software to perform a preliminary processing of the available data, including blanking of the water column, automatic gain control and color enhancement. Even with this simple approach, several interesting features have been observed. Fig. 10 shows two examples of structures identified in the sub-bottom profiler data around Orca seamount. The first profile crosses perpendicularly a N–S linear structure observed in the bathymetry, that emerges from a small cone located NW of Orca volcano. The section shows a well-defined seabed layering, interrupted by an area with no clear reflectors. This area coincides with a topographic high reaching about 37 m above the seafloor and a basal extent of 1.3 km. The materials that make up the promontory have a more chaotic distribution than the surrounding sediments. Further analysis will be required to fully understand this feature, but it could be a radial dyke associated with the volcanic edifice or a perpendicular dyke associated with rifting. The second profile is located in the abyssal plain SE of Orca volcano. We observe a well defined subhorizontal layering, cut by an area with no reflectors and a positive topographic relief with a lateral extent of 830 m and elevation of 15 m. This is the typical morphology of a mud volcano. Although they are usually associated with the emanation of gas produced by the decomposition of organic matter, there are also known cases of mud volcanoes associated with volcanic activity. Future work in this area will focus on elucidating whether this mud volcano is related to volcanic processes.

3.3. Gravity and magnetic data

In addition to regional-to global-scale compilations of satellite and near-surface observations (e.g. Scheinert et al., 2016; Golynsky et al., 2018), there are some studies dealing with the analysis of gravity and magnetic profiles in the Bransfield area (Garrett, 1990; Kim et al., 1992; Gracia et al., 1996; Muñoz-Martín et al., 2005; Yegorova et al., 2011). Combining the information from marine gravity and magnetic surveys, Catalán et al., (2013) produced the most accurate gravity and magnetic anomaly maps of the Bransfield Strait to date, with a grid spacing of 3 km. They find a large-scale gravity high along the rift, reaching about 150 mgal south of King George Island and decreasing SW to values of 100 mgal near Livingston Island. The magnetic anomaly map shows a

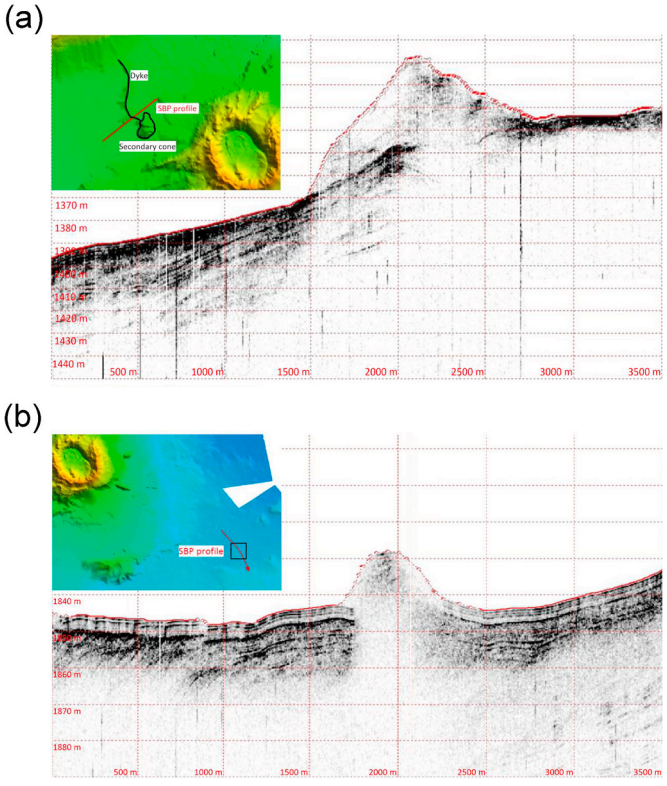

Fig. 10. Examples of the sediment profiler data over two selected targets: a volcanic fissure (a) and a mud volcano (b). The insets show the positions of the SBP profiles relative to Orca volcano.

series of positive anomaly peaks along the Bransfield rift, roughly coincident with volcanic structures such as Humpback, Orca, and the NE side of Three Sisters. However, the relatively sparse navigation lines yield a limited resolution, thus providing a general view of the regional anomalies but making it difficult to associate confidently the anomalies with the particular structures observed on the seafloor.

The BRAVOSEIS dataset has been obtained with dense spatial resolution, especially over Orca and Humpback volcanoes, and we expect that the results can provide insights into their structure and the rift evolution. In order to do that, raw gravity and magnetic data from the 2019 cruise have already been quality-controlled, reduced, and processed, using Oasis Montaj software.

All standard gravity marine corrections were applied to calculate the complete Bouguer anomaly (CBA). For the Eotvos correction, course and speed over ground were provided by the vessel navigation system. The latitude correction was obtained using the Geodetic Reference System 1967. Solid-Earth tides were corrected using Longman's formulation (Longman, 1959). The digital elevation model used for the terrain correction was a combination of a regional grid with a 200-m grid interval (GMRTv6.6, https://doi.org/10.1594/IEDA.100001, Ryan et al., 2009) and the local bathymetry with 15-m grid interval derived from BRAVOSEIS multibeam data. The terrain density value was 2.67 g/cm^3, considering the continental character of the crust in the Bransfield Strait (Catalán et al., 2013). The Bouguer plate correction was obtained with a density of 1.64 g/cm^3 resulting from the difference between 2.67 g/cm^3 used as reduction density and a seawater density of 1.03 g/cm^3. The water slab correction was calculated with the procedures described by Kane (1962), Nagy (1966) and Nettleton (1976). In order to correct herringbone effects and intersection errors related to the systematic acquisition during the oceanographic surveys, a statistical leveling correction will be applied.

Similarly, the magnetic anomaly has been calculated applying standard magnetic data processing. We used the International Geomagnetic Reference Field 2015 (Thebault et al., 2015) to represent the Earth's internal magnetic field. The correction of the external magnetic field contribution (diurnal variation) was carried out using the continuous magnetic data from the permanent geomagnetic station installed on Livingston Island by the Ebre Observatory (Torta et al., 1999; Altadill et al., 2014). To enable an improved location of geomagnetic anomaly sources, we applied a reduction-to-pole (RTP) calculation with an inclination of −55.87° and a declination of 11.1°.

After processing, the valid data were 1,006,339 gravity measurements along 1402 km and 1,167,159 magnetic samples along 2589 km of ship track. Data have been initially interpolated to a resolution of 1 km in all surveyed areas, and to resolution of 100 m in the regions of densest navigation lines (i.e., Orca and Humpback volcanoes) for more detailed analysis.

Fig. 11 shows that the survey area is characterized by a positive CBA between 73 and 166 mgal. Anomaly values reach their minimum around the SW edge of the Central Bransfield Basin near Livingston and Deception Islands, and gradually increase towards the NE. Anomalies around Humpback range from 73 to 116 mgal, while around Orca

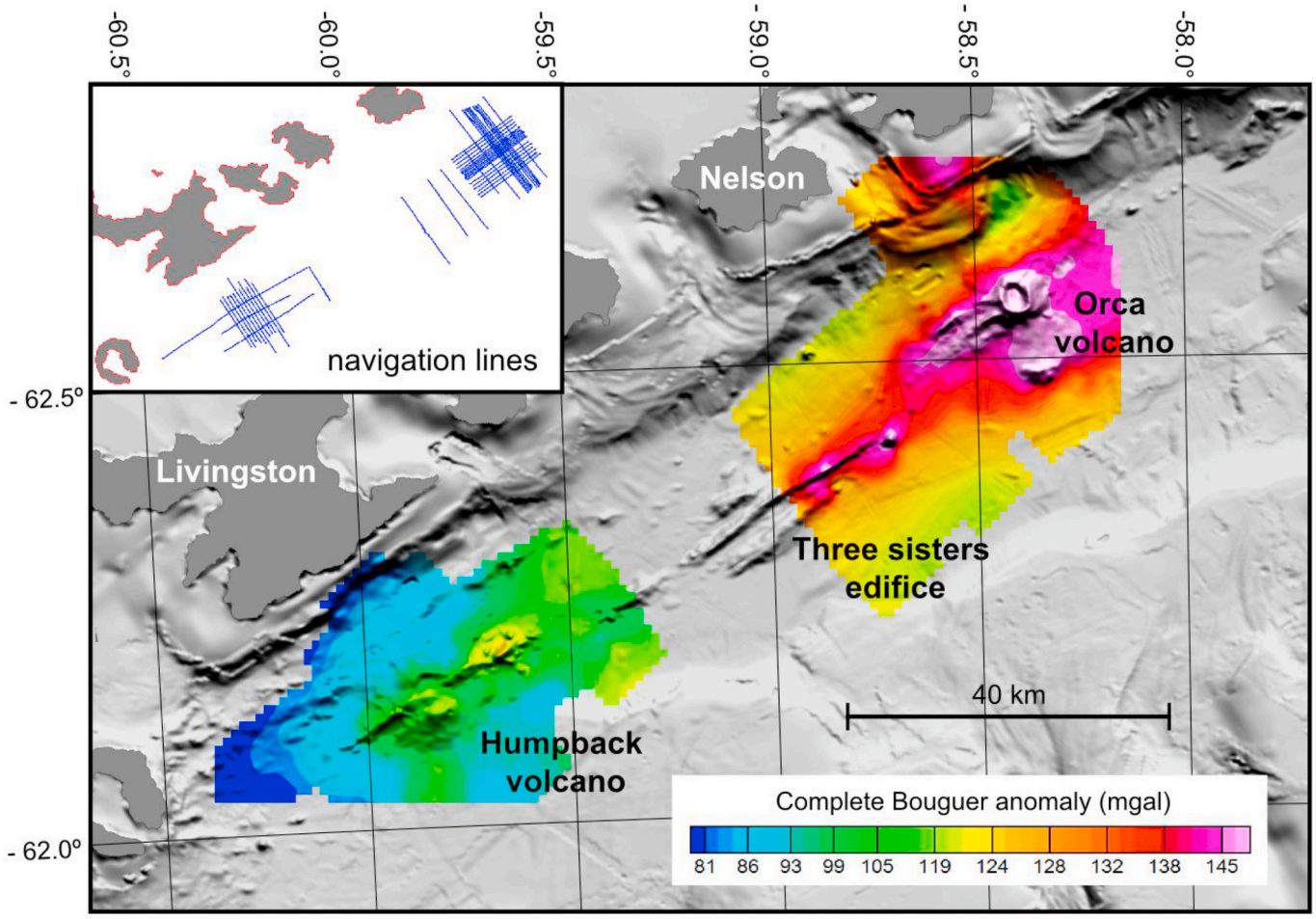

Fig. 11. Complete Bouguer anomaly map of the Central Bransfield Basin using data from the 2019 BRAVOSEIS cruise. Grey-shaded background is a digital elevation model combining GMRT and multibeam data. The inset shows the navigation lines after processing. See color legend form interpretation. (For interpretation of the references to color in this figure legend, the reader is referred to the Web version of this article.)

edifice they extend from 111 to 166 mgal. This difference is consistent with a crust that thins from the SW to the NE in Bransfield Basin due to increasing amounts of accumulated extension (Vuan et al., 2005).

Orca seamount is characterized by a NE-SW elongated maximum that follows the axis of the neovolcanic rift and broadens in the caldera. The gravity maximum extends onto the SE flank of the volcanic edifice and over a small subsidiary ridge located southwards of the caldera, in sharp contrast with the NW flank where it ends abruptly. In the Three Sisters structure, there are two local relative maxima of 145 mgal. One is located on the central ridge, and the other coincides with an adjoining volcanic cone located near the NE tip of the Three Sisters ridge. These maxima might be continuous, although the sparse coverage could make them look like independent features. There is a noticeable 5-km left-lateral offset between the axis of the gravity maximum in Three Sisters and Orca, suggesting the along-strike segmentation of the neovolcanic rift. Humpback seamount is also characterized by a NE-SW trending maximum zone. In this case there are two maxima of >110 mgal. One of them is located in the south part of the caldera, and the other occurs to the NE, over the NE-SW trending, 30 km-long ridge which cross-cuts the Humpback edifice.

The CBA maximum coinciding with the rift in the Bransfield Basin seems to disappear SW towards Deception Island. This may be the case also NE of the Orca edifice where the neovolcanic zone fades at the seafloor. Although our dataset has poorer coverage in these areas, the results match the wider anomaly map of Catalán et al., (2013). The maximum zone located over the neovolcanic axis is flanked NW by a relative minimum that could be related to a progressive crustal thickening towards the offshore island margin (Christeson et al., 2003).

Magnetic anomalies in the survey area vary between −1035 and 1802 nT (Fig. 12). This wide range is consistent with neovolcanic zones over the world (e.g., Taylor, 1995) and with previous studies in this area (Galindo-Zaldívar et al., 2004; Catalán et al., 2013). Positive RTP anomalies define a sinuous elongated maximum that generally follows the axis of the neovolcanic rift. NE of Humpback volcano this feature seems to be interrupted, since there is no positive anomaly in that area, but this might be an artifact of limited coverage and interpolation. The maximum zone broadens over the Orca caldera and extends southeastwards in a similar way to the gravity anomalies, also reaching the small subsidiary ridge located south of Orca. Magnetic anomaly minima are located between the island margin and the neovolcanic axis suggesting a thicker continental-type crust and sedimentary cover (Christeson et al., 2003). As discussed for the gravity anomaly, there are significant differences between the neovolcanic regions of Orca and Humpback volcanoes. Maximum magnetic anomalies are mostly centered over the Orca caldera, but in the case of the Humpback edifice they are located near the ridge ends and not on the caldera. Southwest of the Humpback edifice the positive maximum disappears, although this could be again related to limited data coverage; while northeast of Orca, it seems to continue along a series of small disconnected NE-SW trending ridges.

In order to investigate the depth of the anomaly sources, we calculated the radially averaged power spectrum of the complete Bouguer and RTP magnetic anomalies (Fig. 13). Potential field data, by its nature, include the effects of all the geological sources that can be separated by spectral decomposition (e.g. Spector and Grant, 1970). We carry out the

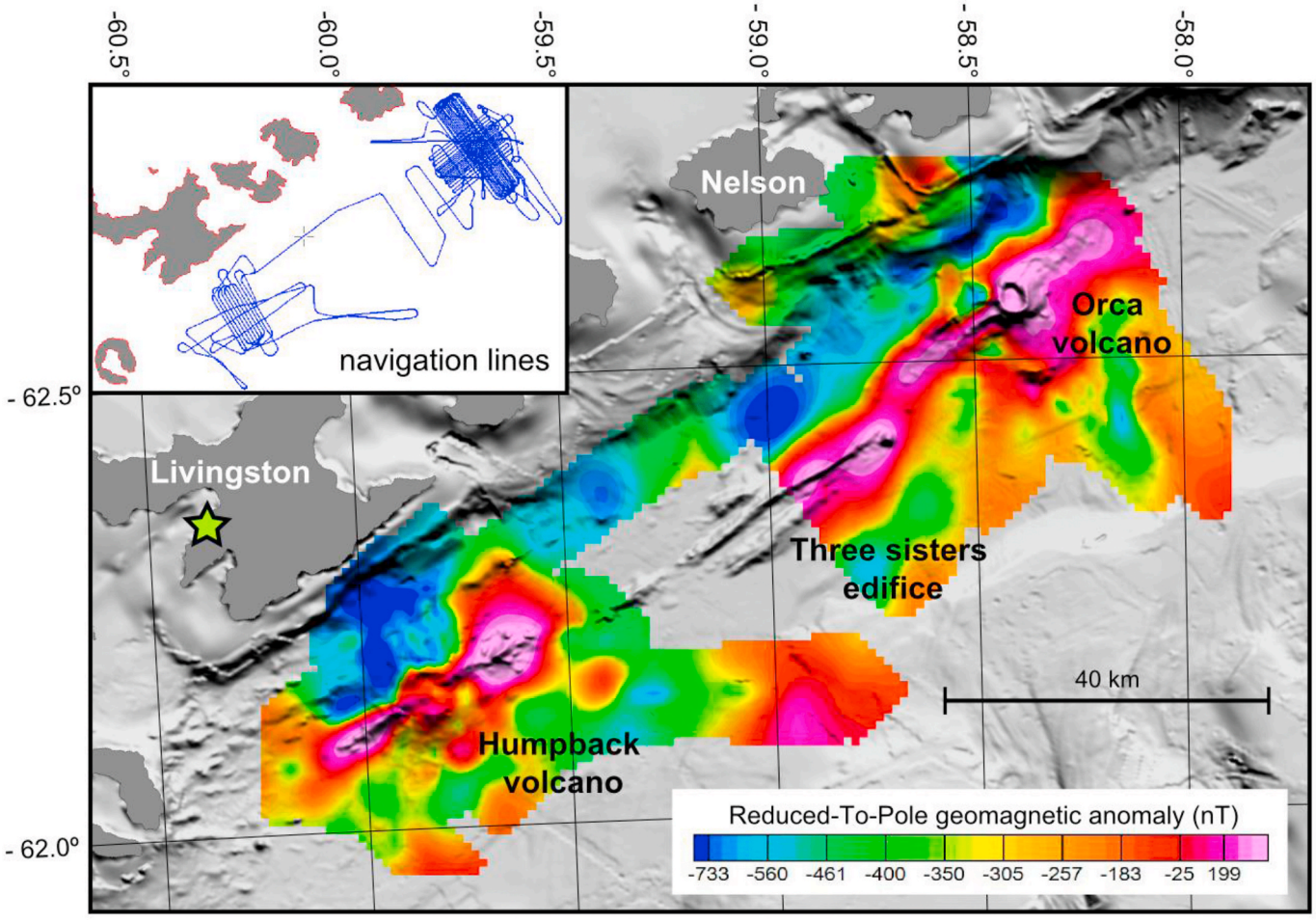

Fig. 12. Same as Fig. 11 for the reduced-to-pole geomagnetic anomaly map of the Central Bransfield Basin. The star shows the location of the permanent geomagnetic station at Livingston Island.

Fourier transform over a regular 100-m grid, in order to keep the high frequency signals yielded by shallower sources. Both CBA and RTP anomaly plots show that the energy spectrum is divided into four linear trends that can be associated with sources at depths that decrease with frequency. The top of the deepest source is located between 2 and 6 km and agrees with the lower-middle crust seismic boundaries identified from deep seismic sounding along the center of the Bransfield strait (Christeson et al., 2003). The top of the intermediate sources in the CBA map at 1–1.5 km is slightly shallower than the depth of 2–2.5 km observed in the RTP map. The top of the shallow sources is 1 km, in agreement with the volcanic bodies observed on the seafloor along the neovolcanic axis. The depth information provided by the spectral decomposition is generic, and will require further gravity and magnetic modeling to interpret.

The patterns shown by the CBA and RTP anomalies evidence notable differences between Orca and Humpback seamounts, and provide insights into the volcanic process. In the case of Orca, we have an elongated maximum suggesting fissural volcanism along the rift. This maximum broadens over the caldera. These features suggest a former stage of fissural volcanism and a later stage of caldera. The anomaly in the SE flank needs to be further modeled but could be related to the magma chamber geometry or some complexity in the spreading pattern. In the case of Humpback, the maximum along the axis of the rift is discontinuous. In the Humpback caldera there is a relative minimum that could be related to the shallowing of Curie isotherm and the consequent loss of the magnetic signature. In this case, the anomaly distribution suggests an earlier stage of caldera formation, and a later stage of fissural volcanism that cross-cuts the caldera rim.

3.4. Active seismic data

Several reflection and refraction seismic studies have been carried out in the Bransfield Strait. Earlier surveys have used 2D MCS reflection profiling to characterize the shallow crustal structure and magmatic history (Gamboa and Maldonado, 1990; Barker and Austin, 1998; Gracia et al., 1996; Galindo-Zaldívar et al., 2004; Okon et al., 2016) and wide-angle seismic tomography to constrain the regional crustal velocity structure at the basin scale (Grad et al., 1997; Christeson et al., 2003; Barker et al., 2003; Janik et al., 2014). Though the results from these studies provide excellent constraints for our investigation, the sparse 2-D profiles were not optimized for resolving finer scale volcanic structures. In our case, the novelty of our work lies in the density of profiles and the frequency characteristics of the air gun array, which can allow for 3D studies and an increased ability to resolve upper crustal structures related to rifting and the potential transition to the formation of new oceanic crust.

Preliminary processing of the MCS profiles has been carried out using the seismic software GLOBEClaritas (V7). We apply an industry-standard processing flow including resampling to 4 ms (with anti-aliasing filter); geometry assignment; muting of the direct and guided waves; brute-stack; amplitude recovery, trace-balance, and band-pass filter (4-6-115-120 Hz); SRME multiple attenuation, predictive deconvolution in tau-p domain; velocity analysis; parabolic Radon transform for residual multiple energy; pre-stack time migration; update of the velocity model; stack; and FX-deconvolution and coherency filter. Some of these techniques are intended for the elimination of multiples (Gomez-Oliveira et al. 2013). In order to identify reflections from deep interfaces, the main challenge is the elimination of these multiples and the improvement of the signal-to-noise ratio. In our case, we operated with a relatively short streamer, in part due to the concerns of navigating in ice-crowded waters; therefore, the attenuation of multiples is a major issue.

As an example of the preliminary results obtained during the processing of the MCS data, we select a ~24 km long profile across the central part of the study zone, over the northeast section of the Three Sisters ridge (Fig. 14a). The profile runs in a SE-NW direction and is perpendicular to the submarine ridge that follows the SW-NE direction of the rift. In Fig. 14b we show the brute stack section, obtained with a constant velocity of 1500 m/s, and the processed section. Two multiples are observed in the stack around 4500 ms and 7000 ms, whose amplitudes are reduced in the processed section and will be reduced further after fine-tuning the processing flow for this specific dataset.

Fig. 14c shows a preliminary interpretation of the seismic section up to 5 s TWT. The central area that forms the relief of the Three Sisters edifice is characterized by a complex superposition of bodies associated with volcanic materials. On both sides of the edifice, we identify a depositional sequence unit, mainly of marine origin (García, 2008; García et al., 2009). It is characterized by a general sub-horizontal stratification. Occasionally sub-vertical discontinuities can be seen cutting partially into this unit. Below the marine sediment unit, a volcano-sedimentary sequence is identified. It shows a sequence of continuous reflectors that describe diverse morphologies, and that are occasionally truncated and cut by vertical faults that grow from the unit situated below. It is interpreted as a syn-rift volcano-sedimentary unit including volcanic, marine, and glacio-marine sediments (Schreider et al., 2015; Okon et al., 2016). The presence of this unit suggests that

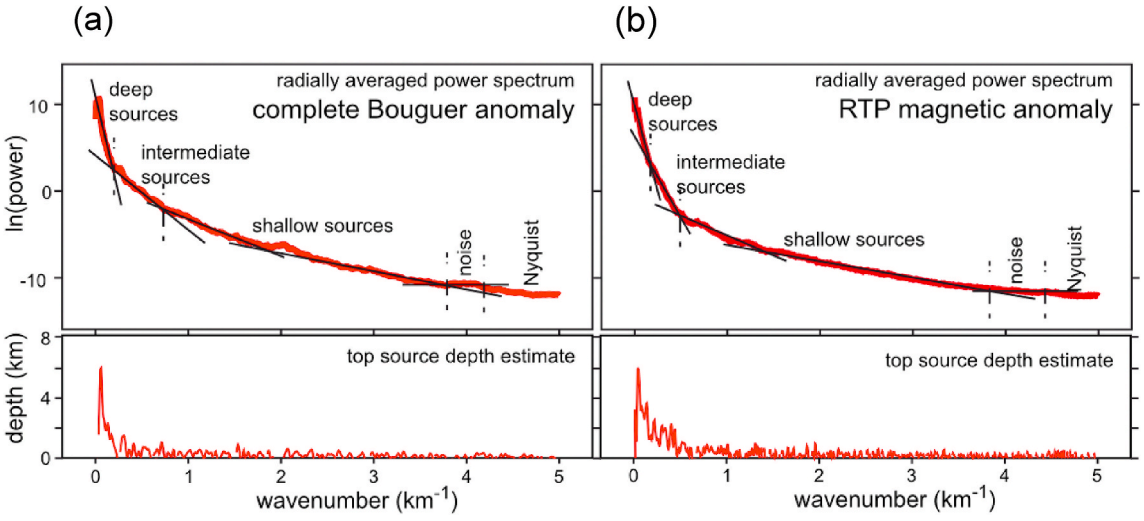

Fig. 13. Radially-averaged power spectra and estimate of top source depth of the anomaly sources. (a) Complete Bouguer anomaly. (b) Reduced-to-pole geomagnetic anomaly.

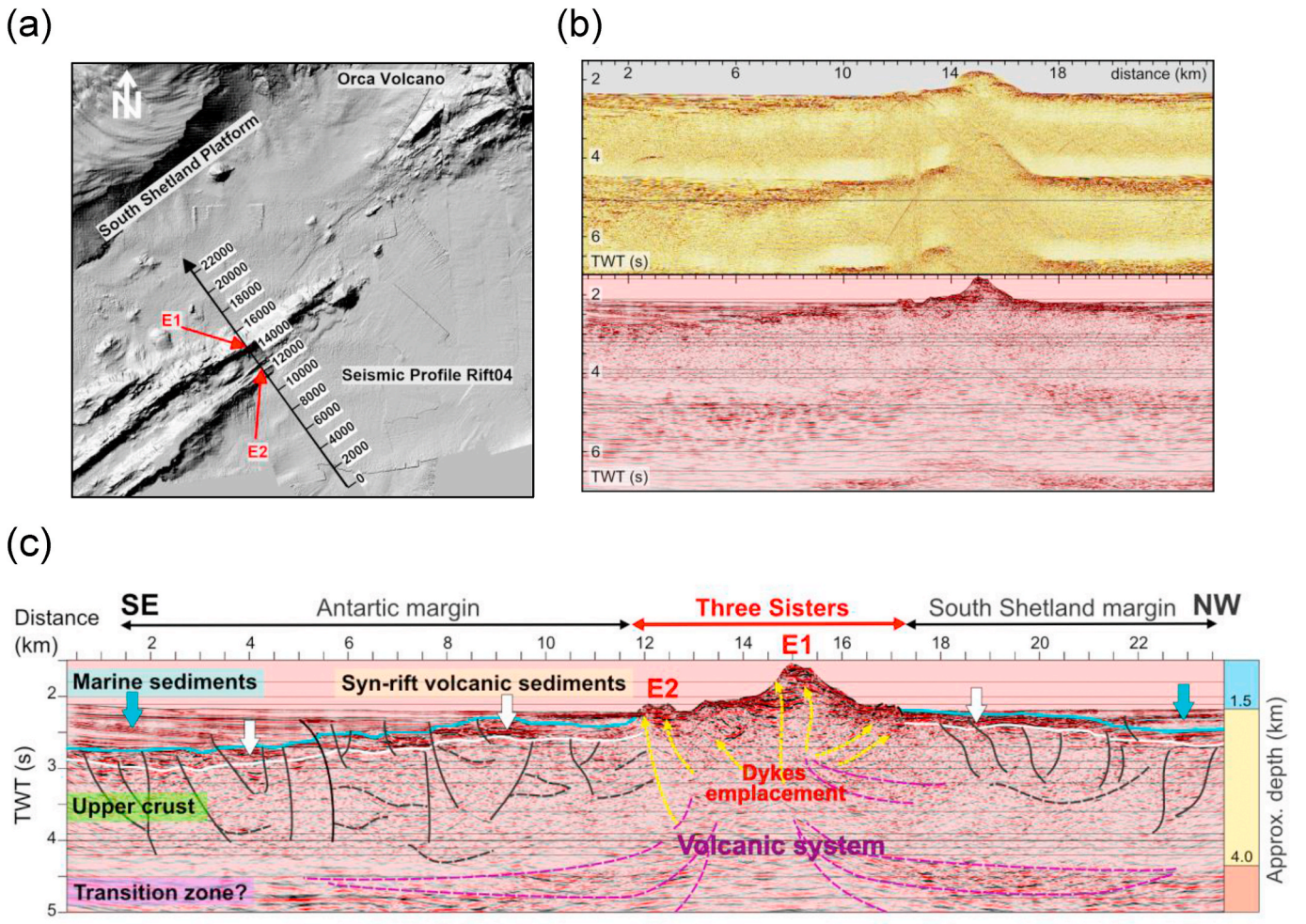

Fig. 14. (a) Location of the seismic profile on the NE part of the Three Sisters structure. The profile is ~24 km long (labels indicate the distance in m) and crosses above two of the main ridges in a direction perpendicular to the rift (E1, E2). (b) Brute stack of seismic profile (top) and result of processing algorithms that reduce the amplitude of multiples (bottom). (c) Resulting seismic section, where we highlight the main velocity contrasts and display a preliminary interpretation (see text for explanations).

volcanic and tectonic activity occurred simultaneously, producing extensional half-graben shaped structures.

Beneath these shallow units, a crystalline basement corresponds to the upper crust. It is a meta-sedimentary (Birkenmajer et al., 1990) crystalline unit, in which we identify vertical discontinuities related to the main faulting systems and horizontal discontinuities that are directly associated with the main deformation structures. Reflectors of greater amplitude and continuity than the upper unit characterize the deepest unit shown in the section (below 4.5 s TWT). Since multiples are significant in this region, a complete interpretation would require further reduction of multiple amplitudes. If this significant change in the response of the medium (lithological-structural and/or rheological change of the materials) is confirmed, it could represent the upper crust - middle crust transition zone. In the central area of the profile coinciding with the Three Sisters edifice, the upper limit of this unit becomes shallower, evidencing the thinning of the upper crust at the rift.

The OBS network on Orca also recorded active seismic data for refraction analyses. A part of the experiment was specifically designed to obtain the 3D velocity structure of the seamount using seismic tomography. Thus, Orca volcano and its western rift zone were densely instrumented with 15 OBS and about 2400 shots were produced at ranges up to 20 km from the caldera (Fig. 6). This configuration will yield >20,000 P-wave travel times for crustal paths, which will allow a high-resolution tomographic model of Orca volcano.

Fig. 15 shows an example of the tomography data recorded in the vicinity of Orca volcano (see Fig. 6). The data is of excellent quality and in general clear crustal P-wave arrivals are visible out to the maximum aperture of the experiment (~20 km) on either the vertical seismometer or hydrophone channel. In the example shown, clear arrivals are largely absent at distances of 4–6 km from the profile center (12–14 km range), likely due to the presence of a highly attenuating region near the summit of Orca volcano which may be linked to the presence of magma or highly altered and fractured crust.

4. Conclusions and future work

This paper describes the development and preliminary results of the BRAVOSEIS project (2017–2020). This experiment has collected a unique, high-quality and multifaceted geophysical data set in the Central Bransfield Basin. Although a lot of analysis remains, the preliminary results provide useful constraints on structure and dynamics of the Bransfield rift and associated volcanoes.

The preliminary earthquake locations for 2018 demonstrate that the region is quite seismically active with earthquakes distributed beneath the South Shetland Trench, the South Shetland Islands, the Bransfield Basin and somewhat surprisingly, the Antarctic Peninsula. A concentration of earthquakes and normal faulting mechanisms along the rift axis suggests that much of the extension is focused in this region but the presence of earthquakes elsewhere in the basin is consistent with a component of back-arc extension being more broadly distributed. The

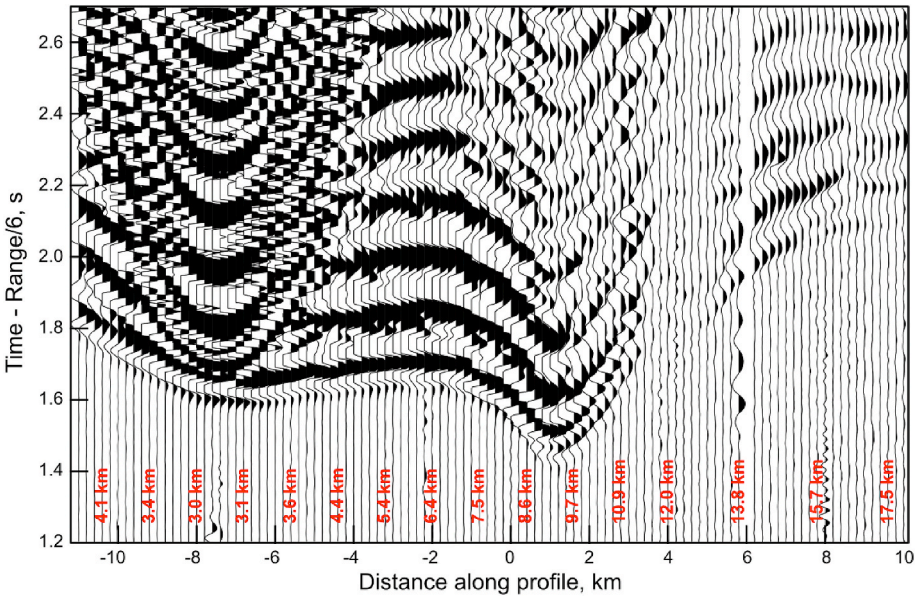

Fig. 15. Example record section plotted with a reduction velocity of 6 km/s for shots along a tomography line, recorded on a short-period OBS (BRA13, see Fig. 6). The data have been filtered with a 5 Hz, 4th-order, high-pass filter and are scaled with range. The horizontal axis shows the shot position along the profile and the red labels indicate the range of the shots. (For interpretation of the references to color in this figure legend, the reader is referred to the Web version of this article.)

2019 regional seismic network comprises more than three times as many sensors within the Basin (including OBSs). Therefore, it should lead to an earthquake catalog with a lower detection threshold, smaller hypocentral uncertainties, and well-constrained focal mechanisms. This seismic data will be used for a range of passive seismic imaging studies including surface and body wave tomography and receiver function analysis. In addition, the local OBS network on Orca volcano will enable a study of microseismicity on a segment of the rift.

Co-deployment of the six hydrophone moorings with the OBS and land seismometers provides a rare opportunity to study seismo-acoustic conversion processes of shallow crustal earthquake phases as they propagate through the seafloor-ocean interface and into the water-column. We will calculate earthquake acoustic magnitudes using T-phases, which will allow us to empirically compare seismic and acoustic magnitudes, phase scattering at the seafloor-ocean interface, magnitude detection thresholds, as well as correlate seismic and acoustic earthquake locations to better constrain earthquake sources and reduce location bias. These analyses should allow us to improve identification of potential submarine volcanic sources within the Bransfield Strait. In addition, we will investigate the cryogenic and biogenic sound sources (icequakes, whales), determine long-term ambient sound trends related to climate effects by comparison to previous sound levels (Dziak et al., 2015), and document human-made sound sources with the goal of assessing their contribution to ambient noise.

The multibeam bathymetric data has yielded high-resolution maps of two volcanic features, Orca and Humpback volcanoes, that demonstrate contrasting eruptive morphologies and structural evolutions that may be linked to a SW to NE increase in accumulated strain within the basin. The availability of sediment profiler data allows for the subsurface characterization of seafloor volcanic and sedimentary structures, which will further enhance the utility of the bathymetric data for interpretations of earthquake patterns and geophysical images of crustal structure.

Additional constraints on the rift structure come from the analysis of potential field data and the spatial distribution of gravity and magnetic anomalies. Our data provide high-resolution anomaly maps, allowing us to associate local anomalies to smaller structures along the neovolcanic zone well imaged with the multibeam bathymetry and seismic data. Gravity and magnetic highs delineate a segmented rift with along axis trends in maximum anomalies, consistent with increased accumulated strain to the NE. At Humpback volcano the combined bathymetry and potential field data suggest that caldera formation preceded the latest episode of rift extension; while at Orca volcano, the caldera appears to have formed after a stage of fissural volcanism. The 2D modeling of the gravity and magnetic profiles, as well as the 3D, will provide insights into the structure of the rift, particularly near the Humpback and Orca seamounts.

We collected an extensive MCS dataset as well as an OBS refraction/tomography dataset on Orca volcano. A processing workflow has been developed for the MCS data that substantially suppresses water column multiples despite the short length of the streamer. A preliminary interpretation of a profile in the Three Sisters region shows that the rift has a complex volcanic structure and that volcanism was accompanied by tectonic and sedimentary processes associated with the formation of grabens and half grabens. Future analysis will focus on refining the processing scheme to further improve the multiple suppression, and on a 3D interpretation of the structure beneath Orca and Humpback volcanoes. The tomography data set on Orca volcano is high quality and demonstrates the presence of a shallow attenuation zone beneath the caldera. It will be used to image the magmatic structure of the volcano and improve microearthquake locations.

The BRAVOSEIS experiment has provided an unprecedented high-resolution geophysical dataset of the Bransfield Strait, especially around Orca and Humpback volcanoes. The combination of results from MCS, tomography, potential field anomaly maps, sediment profiler and bathymetry data, earthquake locations and mechanisms, crustal structure, etc., provide constraints that will yield better results than any of these techniques could do separately. The joint interpretation of the complete dataset, in the framework of previous research performed in this area, will improve our understanding of the structure and dynamics of the Bransfield Basin and the generation of volcanism along the rift.

Declaration of competing interest

The authors declare that they have no known competing financial interests or personal relationships that could have appeared to influence the work reported in this paper.

Acknowledgements

This work has been funded by project BRAVOSEIS (CTM2016-77315-R) of the Spanish Ministry of Science. Additional funds came through the National Science Foundation (ANT-17744651 and ANT-1744581) and the Alfred Wegener Institute. We thank all participants in the BRAVOSEIS 2018, 2019, and 2020 cruises, with a special acknowledgement to Capt. J. E. Regodón and his crew at R/V Hesperides; Capt. J. C. Hernández and his crew at Sarmiento de Gamboa; M. A. Ojeda, E. González, and all the UTM staff involved in the planning and realization of the surveys. They all spared no effort to help us reach our scientific objectives. We also thank the Spanish Polar Committee and institutions involved in the management of the Spanish Antarctic campaigns and the development of the Spanish Polar Program. We are grateful for the help and support that we have always found in the personnel of the Antarctic Bases, especially the Spanish Bases Juan Carlos I and Gabriel de Castilla. We thank the German Instrument Pool for Amphibian Seismology (DEPAS) for providing the temporary onshore stations and the broadband ocean-bottom seismometers. Raw network data are available at GEOFON (network code 5M, Heit et al., 2020) and IRIS (network code ZX, Wilcock et al., 2020) data centers, and can be accessed upon request. This paper is NOAA/Pacific Marine Environmental Laboratory contribution number 5130.

References

Alfred-Wegener-Institut Helmholtz-Zentrum für Polar- und Meeresforschung & GFZ German Research Centre for Geosciences, 2017. DEPAS (Deutscher Geräte-Pool für Amphibische Seismologie): German Instrument Pool for Amphibian Seismology. Journal of Large-Scale Research Facilities 3, A122. https://doi.org/10.17815/jlsrf-3-165.

Almendros, J., Ibáñez, J.M., Alguacil, G., Del Pezzo, E., Ortiz, R., 1997. Array tracking of the volcanic tremor source at Deception Island, Antarctica. Geophys. Res. Lett. 24, 3069–3072. https://doi.org/10.1029/97GL03096.

Almendros, J., Ibáñez, J.M., Alguacil, G., Del Pezzo, E., 1999. Array analysis using circular-wave-front geometry: an application to locate the nearby seismo-volcanic source. Geophys. J. Int. 136, 159–170. https://doi.org/10.1046/j.1365-246X.1999.00699.x.

Almendros, J., Carmona, E., Jiménez-Morales, V., Díaz-Moreno, A., Lorenzo, F., Berrocoso, M., de Gil, A., Fernández-Ros, A., Rosado, B., 2015. Deception Island (Antarctica): sustained deformation and large increase in seismic activity during 2014-2015. In: Venzke, E. (Ed.), Bulletin of the Global Volcanism Network, vol. 40. Smithsonian Institution.

Almendros, J., Carmona, E., Jiménez-Morales, V., Díaz-Moreno, A., Lorenzo, F., 2018. Volcano-tectonic activity at Deception Island volcano following a seismic swarm in the Bransfield rift (2014-2015). Geophys. Res. Lett. 45 (10), 4788–4798. https://doi.org/10.1029/2018gl077490.

Altadill, D., Marsal, S., Blanch, E., Torta, J.M., Quintana-Seguí, P., Solé, J.G., Cid, O., Curto, J.J., Ibáñez, M., Segarra, A., Pijoan, J.L., Juan, J.M., 2014. The livingston island geomagnetic and ionospheric observatory. Geophys. Res. Abstr. 16, EGU2014–4084. EGU General Assembly.

Ashcroft, W.A., 1972. Crustal Structure of the South Shetland Islands and Bransfield Strait. British Antarctic Survey Scientific Reports, vol. 66. British Antarctic Survey, Cambridge, p. 43.

Barclay, A.H., Wilcock, W.S.D., Ibáñez, J.M., 2009. Bathymetric constraints on the tectonic and volcanic evolution of deception island volcano, south shetland islands. Antarct. Sci. 21, 153–167. https://doi.org/10.1017/S0954102008001673.

Barker, D.H., Austin, J.A., 1998. Rift propagation, detachment faulting, and associated magmatism in Bransfield Strait, Antarctic Peninsula. J. Geophys. Res. 103, 24017–24043. https://doi.org/10.1029/98JB01117.

Barker, D.H., Christeson, G.L., Austin, J.A., Dalziel, I.W., 2003. Backarc basin evolution and cordilleran orogenesis: insights from new ocean-bottom seismograph refraction profiling in Bransfield Strait. Antarctica. Geology 31 (2), 107–110. https://doi.org/10.1130/0091-7613(2003)0310107:BBEACO>2.0.CO;2.

Bartolini, S., Geyer, A., Marti, J., Pedrazzi, D., Aguirre-Díaz, G., 2014. Volcanic hazard on deception island (south shetland islands, Antarctica). J. Volcanol. Geoth. Res. 285, 150–168. https://doi.org/10.1016/j.jvolgeores.2014.08.009, 0.

Ben-Zvi, T., Wilcock, W.S.D., Barclay, A.H., Zandomeneghi, D., Ibáñez, J.M., Almendros, J., 2009. The P-wave velocity structure of Deception Island, Antarctica, from two-dimensional seismic tomography. J. Volcanol. Geoth. Res. 180, 67–80. https://doi.org/10.1016/j.jvolgeores.2008.11.020.

Berrocoso, M., Fernández-Ros, A., Prates, G., García, A., Kraus, S., 2016. Geodetic implications on block formation and geodynamic domains in the south shetland islands, antarctic peninsula. Tectonophysics 666, 211–219. https://doi.org/10.1016/j.tecto.2015.10.023.

Birkenmajer, K., Delitala, M.C., Narebski, W., Nicoletti, M., Petrucciani, C., 1986. Geochronology of tertiary island-arc volcanics and glaciogenic deposits, king george island, south shetland islands (west Antarctica). Bull. Pol. Acad. Sci. Earth Sci. 34, 257–273.

Birkenmajer, K., Guterch, A., Grad, M., Janik, T., Perchuc, E., 1990. Lithospheric transect antarctic Peninsula-South shetland islands, west Antarctica. Pol. Polar Res. 11, 241–258.

Biryol, C.B., Lee, S.J., Lees, J.M., Shore, M.J., 2018. Lithospheric structure of an incipient rift basin: results from receiver function analysis of Bransfield Strait, NW Antarctic Peninsula. Polar Science 16, 47–58. https://doi.org/10.1016/j.polar.2018.02.003.

Carbó, A., Muñoz, A., Llanes, P., Alvarez, J., ZEE working group, 2003. Gravity analysis offshore the Canary Islands from a systematic survey. Mar. Geophys. Res. 24, 113–127. https://doi.org/10.1007/s11001-004-1336-2.

Carmona, E., Almendros, J., Martín, R., Serrano, I., Stich, D., Ibáñez, J.M., 2012. Results of seismic monitoring surveys of Deception Island volcano, Antarctica, from 1999-2011. Antarct. Sci. 24, 485–499. https://doi.org/10.1017/S0954102012000314.

Carmona, E., Almendros, J., Martín, R., Cortes, G., Alguacil, G., Moreno, J., Martín, J.B., Martos, A., Serrano, I., Stich, D., Ibáñez, J.M., 2014. Advances in seismic monitoring at deception island volcano (Antarctica) since the international polar year. Ann. Geophys. 57, SS0321. https://doi.org/10.4401/ag-6378.

Catalán, M., Galindo-Zaldívar, J., Martín-Davila, J., Martos, Y.M., Maldonado, A., Gamboa, L., Schreider, A.A., 2013. Initial stages of oceanic spreading in the Bransfield Rift from magnetic and gravity data analysis. Tectonophysics 585, 102–112. https://doi.org/10.1016/j.tecto.2012.09.016.

Christeson, G.L., Barker, D.H.N., Austin, J.A., Dalziel, I.W.D., 2003. Deep crustal structure of Bransfield Strait: initiation of a back arc basin by rift reactivation and propagation. J. Geophys. Res. 108 (B10), 2492. https://doi.org/10.1029/2003JB002468.

Davoli, R., 2019. Análisis de la sismicidad en el Estrecho de Bransfield (Antártida) durante el año 2018 y el principio de 2019. M.Sc. Thesis, Master in Geophysics and Meteorology. University of Granada (in Spanish).

Dietrich, R., Rulke, A., Ihde, J., Lindner, K., Miller, H., Niemeier, W., et al., 2004. Plate kinematics and deformation status of the Antarctic Peninsula based on GPS. Global Planet. Change 42 (1), 313–321. https://doi.org/10.1016/j.gloplacha.2003.12.003.

Dimitrova, L., Georgieva, G., Raykova, R., Dimitrov, D., Gourev, V., Solakov, D., Georgiev, I., Raykova, P., Protopopova, V., Aleksandrova, I., Popova, M., 2017. Exploring seismicity of Livingston Island (Antarctica) and surroundings using records of Bulgarian Broadband Seismological Station LIVV during the astral summer 2015-2016. Comptes Rendus of the Bulgarian Academy of Sciences 70 (12), 1709–1718.

Dziak, R.P., Park, M., Lee, W.S., Matsumoto, H., Bohnenstiehl, D.R., Haxel, J.H., 2010. Tectonomagmatic activity and ice dynamics in the Bransfield Strait back-arc basin, Antarctica. J. Geophys. Res. 115 (B1), B01102. https://doi.org/10.1029/2009JB006295.

Dziak, R.P., Bohnenstiehl, D.R., Stafford, K.M., Matsumoto, H., Park, M., Lee, W.S., 2015. Sources and levels of ambient ocean sound near the Antarctic Peninsula. PloS One 10, e0123425. https://doi.org/10.1371/journal.pone.0123425.

Eagles, G., 2004. Tectonic evolution of the antarctic–phoenix plate system since 15 ma. Earth Planet Sci. Lett. 217 (1–2), 97–109. https://doi.org/10.1016/S0012-821X(03)00584-3.

Fernández-Ros, A.M., Berrocoso, M., Ramirez, M.E., 2007. Volcanic deformation models for deception island (south shetland islands, Antarctica). In: Cooper, A.K., Raymond, C.R. (Eds.), Antarctica: A Keystone in Changing World, Proceedings of the 10th ISAES. USGS Open-File Report 2007-1047. Extended Abstract 094.

Fisk, M.R., 1990. Volcanism in the bransfield strait, Antarctica. J. South Am. Earth Sci. 3 (2–3), 91–101. https://doi.org/10.1016/0895-9811(90)90022-S.

Fretzdorff, S., Worthington, T.J., Haase, K.M., Hekinian, R., Franz, L., Keller, R.A., Stoffers, P., 2004. Magmatism in the bransfield basin: rifting of the south shetland arc? J. Geophys. Res. 109 (B12), B12208. https://doi.org/10.1029/2004JB003046.

Galindo-Zaldívar, J., Gamboa, L., Maldonado, A., Nakao, S., Bochu, Y., 2004. Tectonic development of the bransfield basin and its prolongation to the south scotia ridge, northern antarctic peninsula. Mar. Geol. 206 (1–4), 267–282. https://doi.org/10.1016/j.margeo.2004.02.007.

Galindo-Zaldívar, J., Gamboa, L., Maldonado, A., Nakao, S., Bochu, Y., 2006. Bransfield basin tectonic evolution. In: Futterer, D.K., Damaske, D., Kleinschmidt, G., Miller, H., Tessensohn, F. (Eds.), Antarctica. Springer, pp. 243–248. https://doi.org/10.1007/3-540-32934-X_29.

Gamboa, L.A.P., Maldonado, P.R., 1990. Geophysical investigations in the bransfield strait and in the bellinghausen sea, Antarctica. In: St John, B. (Ed.), Antarctica as an Exploration Frontier: Hydrocarbon Potential, Geology and Hazards. Am. Ass. Petrol. Geol., Studies in Geology, vol. 31, pp. 127–141.

García, M., 2008. Post-rift Sedimentary Evolution of the Central Bransfield Basin (Antarctic Peninsula). Ph.D. Thesis. University of Barcelona, Spain. http://hdl.handle.net/10261/108118.

García, M., Ercilla, G., Alonso, B., 2009. Morphology and sedimentary systems in the Central Bransfield Basin, Antarctic Peninsula: sedimentary dynamics from shelf to basin. Basin Res. 21, 295–314. https://doi.org/10.1111/j.1365-2117.2008.00386.x.

Garrett, S.W., 1990. Interpretation of reconnaissance gravity and aeromagnetic surveys of the Antarctic Peninsula. J. Geophys. Res. 95 (B5), 6759–6777. https://doi.org/10.1029/JB095iB05p06759.

Golynsky, A.V., Ferraccioli, F., Hong, J.K., Golynsky, D.A., von Frese, R.R.B., Young, D. A., Blankenship, D.D., Holt, J.W., Ivanov, S.V., Kiselev, A.V., Masolov, V.N., Eagles, G., Gohl, K., Jokat, W., Damaske, D., Finn, C., Aitken, A., Bell, R.E., Armadillo, E., Jordan, T.A., Greenbaum, J.S., Bozzo, E., Caneva, G., Forsberg, R., Ghidella, M., Galindo-Zaldívar, J., Bohoyo, F., Martos, Y.M., Nogi, Y., Quartini, E., Kim, H.R., Roberts, J.L., 2018. New magnetic anomaly map of the antarctic. Geophys. Res. Lett. 45, 6437–6449. https://doi.org/10.1029/2018GL078153.

Gonzalez-Casado, J.M., Robles, J.L.G., Lopez-Martínez, J., 2000. Bransfield basin, antarctic peninsula: not a normal backarc basin. Geology 28 (11), 1043–1046. https://doi.org/10.1130/0091-7613(2000)281043:BBAPNA>2.0.CO;2.

Gracia, E., Canals, M., Farran, M.-l., Prieto, M.J., Sorribas, J., Gebra Team, 1996. Morphostructure and evolution of the central and eastern bransfield basins (NW antarctic peninsula). Mar. Geophys. Res. 18, 429–448. https://doi.org/10.1007/BF00286088.

Gracia, E., Canals, M., Farran, M.-l., Sorribas, J., Pallas, R., 1997. Central and eastern bransfield basins (Antarctica) from high-resolution swath-bathymetry data. Antarct. Sci. 9 (2), 168–180. https://doi.org/10.1017/S0954102097000229.

Grad, M., Guterch, A., Janik, T., 1993. Seismic structure of the lithosphere across the zone of subducted Drake plate under the Antarctic plate, West Antarctica, Geophys. J. Intell. 115, 586–600. https://doi.org/10.1111/j.1365-246X.1993.tb01209.x.

Grad, M., Shiobara, H., Janik, T., Guterch, A., Shimamura, H., 1997. Crustal model of the Bransfield Rift, West Antarctica, from detailed OBS refraction experiments. Geophys. J. Int. 130 (2), 506–518. https://doi.org/10.1111/j.1365-246X.1997.tb05665.x.

Heit, B., Yuan, X., Almendros, J., Abella, R., Carmona, E., Aguí, F., Carrión, P., 2020. BRAVOSEIS Onshore Seismic Array. GFZ Data Services. https://doi.org/10.14470/0Z7563857972.

Henriet, J.P., Meissner, R., Miller, H., GRAPE Team, 1992. Active margin processes along the antarctic peninsula. Tectonophysics 201, 229–253. https://doi.org/10.1016/0040-1951(92)90235-X.

Ibáñez, J.M., Almendros, J., Carmona, E., Martínez-Arevalo, C., Abril, M., 2003. The recent seismo-volcanic activity at Deception Island volcano. Deep Sea Research II 50 (10–11), 1611–1629. https://doi.org/10.1016/S0967-0645(03)00082-1.

Ibáñez, J.M., Del Pezzo, E., Almendros, J., La Rocca, M., Alguacil, G., Ortiz, R., García, A., 2000. Seismovolcanic signals at Deception Island volcano, Antarctica: wave field analysis and source modeling. J. Geophys. Res. 105, 13905–13931. https://doi.org/10.1029/2000JB900013.

Ibáñez, J.M., Morales, J., Alguacil, G., Almendros, J., Ortiz, R., Del Pezzo, E., 1997. Intermediate-focus earthquakes under south shetland islands, Antarctica. Geophys. Res. Lett. 24 (5), 531–534. https://doi.org/10.1029/97GL00314.

Ibáñez, J.M., Díaz-Moreno, A., Prudencio, J., Zandomeneghi, D., Wilcock, W., Barclay, A., Almendros, J., Benítez, C., García-Yeguas, A., Alguacil, G., 2017. Database of multi-parametric geophysical data from the TOMODEC experiment on Deception Island, Antarctica. Scientific Data 4, 170128. https://doi.org/10.1038/sdata.2017.128.

International Seismological Centre, 2020. On-line Bulletin. https://doi.org/10.31905/D808B830.

Janik, T., Sroda, P., Grad, M., Guterch, A., 2006. Moho depth along the antarctic peninsula and crustal structure across the landward projection of the hero fracture zone. In: Futterer, D.K., Damaske, D., Kleinschmidt, G., Miller, H., Tessensohn, F. (Eds.), Antarctica: Contributions to Global Earth Sciences. Springer, pp. 229–236. https://doi.org/10.1007/3-540-32934-X_27.

Janik, T., Grad, M., Guterch, A., Sroda, P., 2014. The deep seismic structure of the Earth's crust along the Antarctic Peninsula: a summary of the results from Polish geodynamical expeditions. Part B Global and Planetary Change, Scotia Arc evolution: Global implications 123, 213–222. https://doi.org/10.1016/j.gloplacha.2014.08.018. doi.

Jiménez-Morales, V., Almendros, J., Carmona, E., 2017. Detection of long-duration tremors at Deception Island volcano, Antarctica. J. Volcanol. Geoth. Res. 347, 234–249. https://doi.org/10.1016/j.jvolgeores.2017.09.016.

Kane, M.F., 1962. A comprehensive system of terrain corrections using a digital computer. Geophysics 27 (4), 455–462. https://doi.org/10.1190/1.1439044.

Keller, R.A., Fisk, M.R., Smellie, J.L., Strelin, J.A., Lawver, L.A., 2002. Geochemistry of back arc basin volcanism in Bransfield Strait, Antarctica: subducted contributions and along-axis variations. J. Geophys. Res. 107 (B8), 2171. https://doi.org/10.1029/2001JB000444.

Kepleis, K., Lawver, L., 1994. Bathymetry of the bransfield strait, southeastern shackleton fracture zone, and south shetland trench, Antarctica. Antarctic Journal of the US 28, 103–105.

Kim, Y., Chung, T.W., Nam, S.H., 1992. Marine magnetic anomalies in bransfield strait, Antarctica. In: Yoshida, Y., et al. (Eds.), Recent Progress in Antarctic Earth Science, pp. 431–437.

Klinkhammer, G., Chin, C., Keller, R., Dahlmann, A., Sahling, H., Sarthou, G., Petersen, S., Smith, F., Wilson, C., 2001. Discovery of new hydrothermal vent sites in Bransfield Strait, Antarctica. Earth Planet Sci. Lett. 193 (3–4), 395–407. https://doi.org/10.1016/S0012-821X(01)00536-2.

Lawver, L., Keller, R., Fisk, M., Strelin, J., 1995. Bransfield strait, antarctic peninsula. Active extension behind a dead arc. In: Taylor, B. (Ed.), Backarc Basins: Tectonics and Magmatism. Springer, pp. 315–342. https://doi.org/10.1007/978-1-4615-1843-3_8.

Lawver, L., Sloan, B., Barker, D., Ghidella, M., Von Herzen, R., Keller, R., Klinkhammer, G., Chin, C., 1996. Distributed, active extension in bransfield basin, antarctic peninsula: evidence from multibeam bathymetry. GSA Today (Geol. Soc. Am.) 6 (11), 1–6.

Longman, I.M., 1959. Formulas for computing the tidal accelerations due to the Moon and the Sun. J. Geophys. Res. 64 (12), 2351–2355. https://doi.org/10.1029/JZ064i012p02351.

Maestro, A., Somoza, L., Rey, J., Martínez-Frias, J., Lopez-Martínez, J., 2007. Active tectonics, fault patterns, and stress field of Deception Island: a response to oblique convergence between the Pacific and Antarctic plates. J. South Am. Earth Sci. 23 (2–3), 256–268. https://doi.org/10.1016/j.jsames.2006.09.023.

Maldonado, A., Dalziel, I.W.D., Leat, P.T., 2015. The global relevance of the Scotia Arc: an introduction. Global Planet. Change 125, A1–A8. https://doi.org/10.1016/j.gloplacha.2014.06.011.

Martinez, F., Okino, K., Ohara, Y., Reysenbach, A.-L., Goffredi, S.K., 2007. back-arc basins. Oceanography 20. https://doi.org/10.5670/oceanog.2007.85.

Muñoz-Martín, A., Catalán, M., Martín-Davila, J., Carbo, A., 2005. Upper crustal structure of Deception Island area (Bransfield Strait, Antarctica) from gravity and magnetic modelling. Antarct. Sci. 17, 213–224. https://doi.org/10.1017/S0954102005002622.

Nagy, D., 1966. The gravitational attraction of a right rectangular prism. Geophysics 31 (2), 362–371.

Nettleton, L.L., 1976. Gravity and Magnetics in Oil Prospecting. MacGraw-Hill, New York.

Newhall, C., Dzurisin, D., 1988. Deception island. In: Historical Unrest at Large Calderas of the World, Volume USGS Bulletin 1855. U.S. Geological Survey, pp. 1013–1019.

Okon, J., Gizejewski, J., Janik, T., 2016. New geological interpretation of multi-channel seismic profiles from the Pacific Margin of the Antarctic Peninsula. Pol. Polar Res. 37, 243–268. https://doi.org/10.1515/popore-2016-0014.

Ortiz, R., García, A., Aparicio, A., Blanco, I., Felpeto, A., Del-Rey, R., Villegas, M.T., Ibáñez, J.M., Morales, J., Del Pezzo, E., Olmedillas, J.C., Astiz, M., Vila, J., Ramos, M., Viramonte, J.G., Risso, C., Caselli, A., 1997. Monitoring of the volcanic activity of deception island, south shetland islands, Antarctica (1986-1995). In: Ricci, C.A. (Ed.), The Antarctic Region: Geological Evolution and Processes. Terrapub, pp. 1071–1076.

Ottemöller, L., Voss, P., Havskov, J., 2017. SEISAN Earthquake Analysis Software for Windows, Solaris, Linux, and MacOSX.

Parera-Portell, J.A., Mancilla, F., Morales, J., Almendros, J., 2020. Structure of the Crust and Upper Mantle beneath the Bransfield Strait (Antarctica) Using P Receiver Functions (submitted to Tectonophysics).

Park, Y., Kim, K.-H., Lee, J., Yoo, H.J., Plasencia, L.M.P., 2012. P-wave velocity structure beneath the northern Antarctic Peninsula: evidence of a steeply subducting slab and a deep-rooted low-velocity anomaly beneath the central Bransfield Basin. Geophys. J. Int. 191 (3), 932–938. https://doi.org/10.1111/j.1365-246X.2012.05684.x.

Pelayo, A.M., Wiens, D.A., 1989. Seismotectonics and relative plate motions in the Scotia Sea region. J. Geophys. Res. 94 (B6), 7293–7320. https://doi.org/10.1029/JB094iB06p07293.

Prieto, M.J., Canals, M., Ercilla, G., De Batist, M., 1998. Structure and geodynamic evolution of the Central Bransfield Basin (NW Antarctica) from seismic reflection data. Mar. Geol. 149 (1–4), 17–38. https://doi.org/10.1016/S0025-3227(98)00038-3.

Robertson-Maurice, S.D., Wiens, D.A., Shore, P.J., Vera, E., Dorman, L.M., 2003. Seismicity and tectonics of the south shetland islands and bransfield strait from a regional broadband seismograph deployment. J. Geophys. Res. 108 (B10), 2461. https://doi.org/10.1029/2003JB002416.

Ryan, W.B.F., Carbotte, S.M., Coplan, J., O'Hara, S., Melkonian, A., Arko, R., Weissel, R. A., Ferrini, V., Goodwillie, A., Nitsche, F., Bonczkowski, J., Zemsky, R., 2009. Global Multi-Resolution Topography (GMRT) synthesis data set. G-cubed 10, Q03014. https://doi.org/10.1029/2008GC002332.

Scheinert, M., Ferraccioli, F., Schwabe, J., Bell, R., Studinger, M., Damaske, D., Jokat, W., Aleshkova, N., Jordan, T., Leitchenkov, G., Blankenship, D.D., Damiani, T.M., Young, D., Cochran, J.R., Richter, T.D., 2016. New Antarctic gravity anomaly grid for enhanced geodetic and geophysical studies in Antarctica. Geophys. Res. Lett. 43, 600–610. https://doi.org/10.1002/2015GL067439.

Schreider, A., Schreider, A., Galindo-Zaldívar, J., Maldonado, A., Gamboa, L., Martos, Y., Lobo, F., Evsenko, E., 2015. Structure of the Bransfield strait crust. Oceanology 55 (1), 112–123. https://doi.org/10.1134/S0001437014060101.

Smellie, J.L., 1990. D. Graham land and south shetland islands. In: LeMasurier, W., Thomson, J., Baker, P., Kyle, P., Rowley, P., Smellie, J., Verwoerd, W. (Eds.), Volcanoes of the Antarctic Plate and Southern Oceans, vol. 48. Antarctic Research Series, pp. 302–359 (AGU).

Spector, A., Grant, F.S., 1970. Statistical models for interpreting aeromagnetic data. Geophysics 35, 293–302. https://doi.org/10.1190/1.1440092.

Taylor, B. (Ed.), 1995. Backarc Basins: Tectonics and Magmatism. Springer, New York, p. 524.

Taylor, F.W., Bevis, M.G., Dalziel, I.W.D., Smalley Jr., R., Frohlich, C., Kendrick, E., Foster, J., Phillips, D., Gudipati, K., 2008. Kinematics and segmentation of the south shetland islands - bransfield basin system, northern antarctic peninsula. G-cubed 9 (4). https://doi.org/10.1029/2007GC001873.

Thebault, E., Finlay, C.C., Beggan, C.D., Alken, P., Aubert, J., et al., 2015. International geomagnetic reference field: the 12th generation. Earth Planets Space 67, 79. https://doi.org/10.1186/s40623-015-0228-9.

Torta, J.M., Gaya-Piqué, L.R., Sole, J.G., Blanco, I., García, A., 1999. A new geomagnetic observatory at Livingston Island (South Shetland Islands): implications for future regional magnetic surveys. Ann. Geophys. 42 (2), 141–151. https://doi.org/10.4401/ag-3709.

Vuan, A., 2001. Joint inversion of receiver function of teleseismic body waves and local group velocity dispersion curves beneath ESPZ and PMSA stations (Antarctic Peninsula). Terra Antartica 8 (1–2), 49–54.

Vuan, A., Robertson-Maurice, S., Wiens, D., Panza, G., 2005. Crustal and upper mantle S-wave velocity structure beneath the Bransfield Strait (West Antarctica) from regional surface wave tomography. Tectonophysics 397 (3–4), 241–259. https://doi.org/10.1016/j.tecto.2004.12.011.

Yegorova, T., Bakhmutov, V., Janik, T., Grad, M., 2011. Joint geophysical and petrological models for the lithosphere structure of the Antarctic Peninsula continental margin. Geophys. J. Int. 184 (1), 90–110. https://doi.org/10.1111/j.1365-246X.2010.04867.x.

Zandomeneghi, D., Barclay, A., Almendros, J., Ibáñez, J.M., Wilcock, W.S.D., Ben-Zvi, T., 2009. Crustal structure of Deception Island volcano from P wave seismic

tomography: tectonic and volcanic implications. J. Geophys. Res. 114, B06310. https://doi.org/10.1029/2008JB006119.